Article

Current Biology

Migration Speed of Cajal-Retzius Cells Modulated by Vesicular Trafficking Controls the Size of Higher-Order Cortical Areas

Graphical Abstract

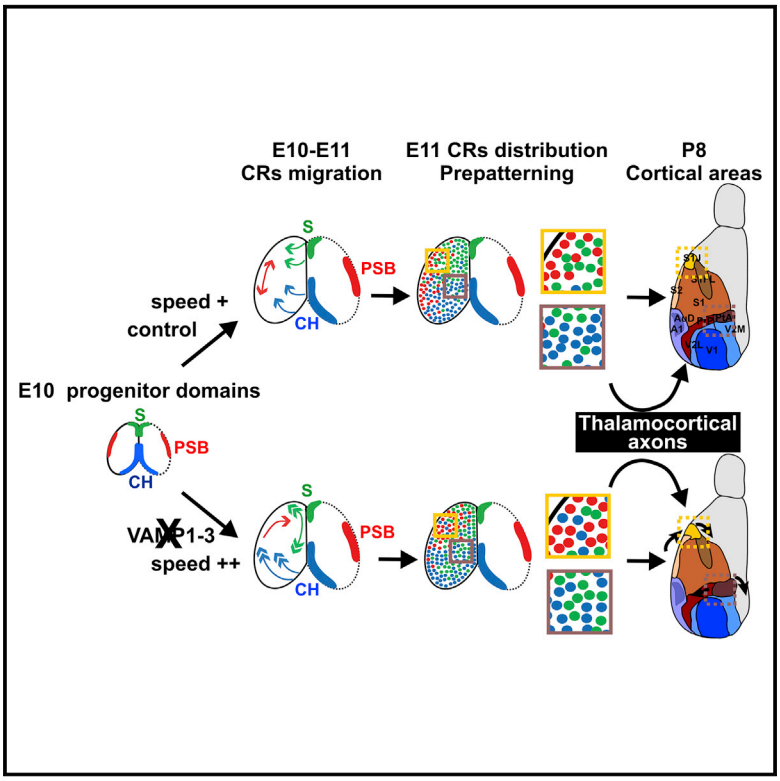

Authors

Melissa Barber, Yoko Arai, Yoshihiro Morishita, ..., Véronique Proux-Gillardeaux, Thierry Galli, Alessandra Pierani

Correspondence

alessandra.pierani@ijm.fr

In Brief

Barber et al. find that vesicular trafficking modulates the migration speed and cortical distributions of Cajal-Retzius neurons. They show that CR composition influences the size and wiring of postnatal visual, auditory, and somatosensory systems. These findings implicate VAMP3 in CR migration and in the patterning of higher-order cortical areas.

Highlights

- Subtype-specific migration kinetics determine CRs cortical distributions
- Inhibiting VAMP3 increases migration speed, but not directionality, of CR subtypes
- VAMP3-dependent vesicular trafficking regulates CR cortical dispersion
- Altered CRs distribution changes the size and wiring of higher-order cortical areas

Barber et al., 2015, Current Biology *25*, 2466–2478
October 5, 2015
http://dx.doi.org/10.1016/j.cub.2015.08.028

CellPress

Current Biology
Article

Migration Speed of Cajal-Retzius Cells Modulated by Vesicular Trafficking Controls the Size of Higher-Order Cortical Areas

Melissa Barber,[1] Yoko Arai,[1] Yoshihiro Morishita,[2] Lisa Vigier,[1] Frédéric Causeret,[1] Ugo Borello,[3] Fanny Ledonne,[1] Eva Coppola,[1] Vincent Contremoulins,[1,4] Frank W. Pfrieger,[5] Fadel Tissir,[6] Subashika Govindan,[7] Denis Jabaudon,[7] Véronique Proux-Gillardeaux,[1,8] Thierry Galli,[1,8] and Alessandra Pierani[1,*]

[1]Institut Jacques Monod, CNRS UMR 7592, Université Paris Diderot, Sorbonne Paris Cité, 75205 Paris Cedex, France
[2]RIKEN Center for Developmental Biology, Kobe 650-0047, Japan
[3]Stem-cell and Brain Research Institute, INSERM U846, 69675 Bron and University of Lyon I, 69003 Lyon, France
[4]ImagoSeine, Institut Jacques Monod, CNRS UMR 7592, Université Paris Diderot, Sorbonne Paris Cité, 75205 Paris Cedex, France
[5]CNRS UPR 3212, University of Strasbourg, Institute of Cellular and Integrative Neurosciences (INCI), 67084 Strasbourg, France
[6]University of Louvain Medical School, Institute of Neuroscience, 1200 Brussels, Belgium
[7]Department of Basic Neurosciences, Faculty of Medicine, University of Geneva, 1211 Geneva, Switzerland
[8]Université Paris Diderot, Sorbonne Paris Cité, INSERM ERL U950, "Membrane Traffic in Health and Disease," 75013 Paris, France
*Correspondence: alessandra.pierani@ijm.fr
http://dx.doi.org/10.1016/j.cub.2015.08.028

SUMMARY

In the neocortex, higher-order areas are essential to integrate sensory-motor information and have expanded in size during evolution. How higher-order areas are specified, however, remains largely unknown. Here, we show that the migration and distribution of early-born neurons, the Cajal-Retzius cells (CRs), controls the size of higher-order areas in the mouse somatosensory, auditory, and visual cortex. Using live imaging, genetics, and in silico modeling, we show that subtype-specific differences in the onset, speed, and directionality of CR migration determine their differential invasion of the developing cortical surface. CR migration speed is cell autonomously modulated by vesicle-associated membrane protein 3 (VAMP3), a classically non-neuronal mediator of endosomal recycling. Increasing CR migration speed alters their distribution in the developing cerebral cortex and leads to an expansion of postnatal higher-order areas and congruent rewiring of thalamo-cortical input. Our findings thus identify novel roles for neuronal migration and VAMP3-dependent vesicular trafficking in cortical wiring.

INTRODUCTION

The neocortex is classically divided into primary areas that process sensory inputs and execute motor commands, and higher-order areas that are essential for the integration of sensory-motor information and cognitive functions. Higher-order areas reside between primary areas and include secondary and association areas that compose most of the human neocortex [1]. These are functionally essential, but their study has been rendered difficult due to their small size in the mouse. While broad patterning of the neocortex into primary areas is regulated by morphogens and gradients of transcription factors at embryonic stages [2, 3], the mechanisms controlling the differentiation of higher-order areas are largely unexplored. Recent studies have revealed that sensory inputs conveyed by thalamocortical axons during postnatal life drive the distinction between primary and higher-order areas [4, 5]. However, it remains unknown whether the delineations between primary and higher-order areas are specified at embryonic stages and, in particular, what determines the final size of higher-order areas.

Cajal-Retzius cells (CRs) are the first born glutamatergic neurons in the embryonic mouse cerebral cortex and occupy the most superficial layer [6–8]. They are best known for their role in regulating cortical lamination through their secretion of Reelin [9–11]. In addition, at embryonic stages CRs have been proposed to regulate the radial glia phenotype [12, 13], the differentiation of upper layers neurons [14], the development of hippocampal connections [15], and the temporal control of interneuron migration [16]. Postnatally, CRs are embedded into immature circuits where they receive GABAergic synaptic inputs and present long-range horizontal projections [17–20] prior to their disappearance around P14. Altogether, these properties suggest that CRs constitute an important component of maturing cortical networks.

Work over the past years has shown that CRs comprise molecularly distinct subtypes that are generated from at least three focal sources at the borders of the developing cortex or pallium: the ventral pallium at the pallial-subpallial boundary (PSB), the pallial septum, and the cortical hem [21–24]. CR subtypes tangentially migrate at a time when the neuroepithelium is regionalized (E10.5–E12.5) and cover the cortical surface by the onset of neurogenesis. CR subtypes invade complementary territories and maintain highly specific distributions in the marginal zone [23–25]. Their early regional distribution coincides with spatial patterning of the cortical primordium, which is required for the formation of functional areas in postnatal mice [2, 3]. We have previously shown by genetic ablation of septum-derived CRs, the role of this subpopulation in regulating the position of the primary motor cortex by signaling to cortical progenitors [25]. This

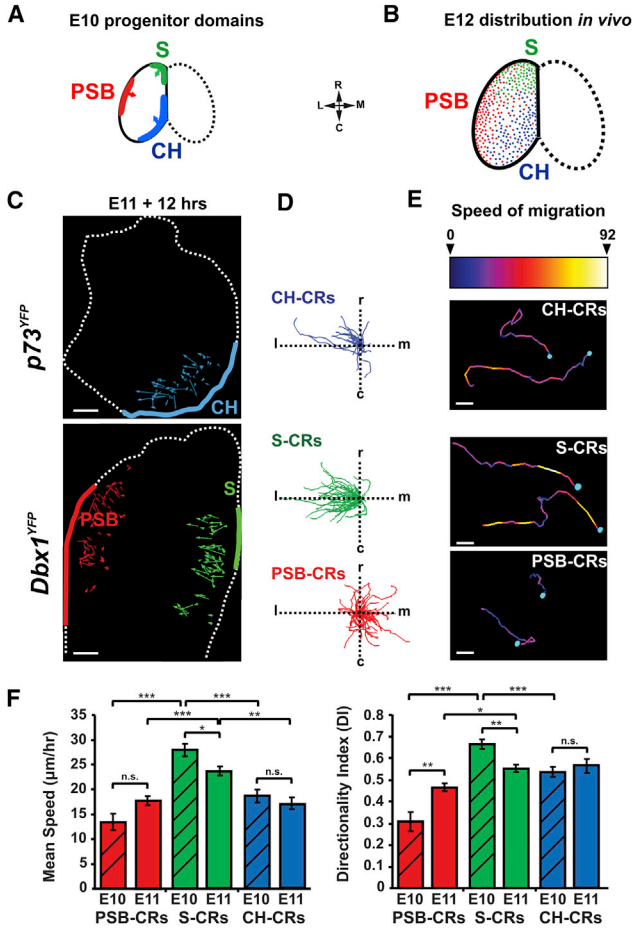

Figure 1. Subtype-Specific Differences in Speed of Migration and Directionality Contribute to the Differential Distribution of CRs in Cortical Territories

(A) CR progenitor domains: the pallial septum (S, green), cortical hem (CH, blue), and ventral pallium at the pallial-subpallial boundary (PSB, red) [22–24].

(B) In vivo complementary distribution of CR subtypes in cortical territories at E12 (taken from [23, 25]): S-CRs (DeltaNp73^{+}Dbx1^{+}, green dots), CH-CRs (DeltaNp73^{+}Dbx1^{-}, blue dots), and PSB-CRs (DeltaNp73^{-}Dbx1^{+}, red dots).

(C) Displacement vectors of CR cells imaged over 12 hr in E11 *p73*^{YFP} and *Dbx1*^{YFP} whole flattened cortical preparations. CH-CRs (n = 46); S-CRs (n = 58); PSB-CRs (n = 69).

(D) Directionality of trajectories at E11 clustered at a common start point.

(E) Representative tracks of migrating CR subtypes at E10 color coded for speed of migration (blue circle: starting position of tracking) showing that S-CR subtypes spend longer time migrating at ≥50 μm/hr (yellow) and at ≥80 μm/hr (white).

(F) Mean speed of migration and directionality index (DI) (ratio of track displacement length to total path length) of CR subtypes from *Dbx1*^{YFP} (PSB-CRs [red columns] and S-CRs [green columns]) and *p73*^{YFP} (CH-CRs [blue columns]) at E10 (hatched columns) and E11 (solid columns). E10: S-CRs (n = 97), CH-CRs (n = 85), PSB-CRs (n = 18); E11: S-CRs (n = 228), PSB-CRs (n = 147), CH-CRs (n = 81). Values show mean ± SEM; unpaired two-tailed t test *p < 0.05, **p < 0.01, ***p < 0.001.

See also Figure S1.

suggested that the presence and/or composition of CRs at the cortical surface are important for the differentiation of underlying neural circuits. At present, little is known on whether subtype-specific differences in CR migration regulate their cortical distribution and, moreover, whether their specific repartition influences the patterning of higher-order cortical areas.

Here, we show that CR subtype-specific differences in migration kinetics determine their specific coverage of the surface of the developing mouse cortex. Furthermore, we reveal that VAMP3-dependent vesicle trafficking cell-autonomously modulates CRs migration speed and their distribution in specific embryonic cortical territories, which, in turn, influences the size and connectivity of higher-order cortical areas in the postnatal cerebral cortex.

RESULTS

Subtype-Specific Differences in Migration Kinetics of CRs Determine Their Differential Invasion of Cortical Territories

Molecularly distinct CR subtypes are generated by three progenitor domains at the borders of the developing mouse cerebral cortex: the pallial septum (S), the cortical hem (CH), and the ventral pallium at the pallial-subpallial boundary (PSB) [22–24] (Figure 1A). Starting at E10, CR subtypes invade the surface of the embryonic cortex by tangential migration. CRs cover the entire cortical sheet at E12 with distinct subpopulations colonizing specific regions: S-CRs (green dots) the rostro-medial, CH-CRs (blue dots) the caudal, and PSB-CRs (red dots) the lateral cortex (Figure 1B) [23, 25].

To investigate how the distribution of CR subtypes is achieved, we genetically traced their migration from their respective sources using a new live-imaging assay on whole flattened cortical vesicles. CR subtypes were labeled with transgenic expression of fluorescent proteins by specific promoters. CH-CRs departing from the caudo-medial (blue) progenitor domain were labeled using *DeltaNp73*$^{Cre/+}$*;ROSA26*$^{YFP/+}$ [26] (hereafter called *p73*^{YFP}), whereas S-CRs and PSB-CRs departing from rostro-medial (green) and lateral (red) progenitor domains, respectively, were labeled with *Dbx1*$^{Cre/+}$*;ROSA26*$^{YFP/+}$ [23, 25] (hereafter called *Dbx1*^{YFP}) (Figures 1C, S1A, and S1D). S-CRs were also traced with the *p73*^{YFP} transgenic line and behaved similarly to S-CRs from the *Dbx1*^{YFP} line (Figures S1A–S1I). Time-lapse analysis from E10 onward showed that S-CRs initiated directed tangential migration before PSB-CRs and CH-CRs (Figures S1A–S1G; Movie S1). By E11, all subtypes migrated extensively from their sources (Figures 1C, S1H, and S1I; Movies S1 and S2). Directed long distance migration originated exclusively from the edges of the cortical explants, whereas YFP^{+} cells in central regions of the explants from both transgenic lines exhibited minimal displacement (Figures S1J and S1K) but actively extended protrusions exploring their environment (Movie S2). This suggested that earlier streams of CRs stopped migrating when reaching the dorsal pallium and streams of later-arriving CRs fill up available space within the expanding dorsal cortex. Clustering of reconstructed cell tracks to a common origin (Figure 1D) showed a clear lateral bias in the directionality of S-CRs and CH-CRs toward the dorsal cortex, in contrast to PSB-CRs, which also migrated along the rostro-caudal axis. Strikingly, from the onset of migration, S-CRs migrated significantly faster than other CRs and along more linear trajectories, as measured by their directionality index (DI) (Figures 1E and 1F). Thus, CR populations differ in migration

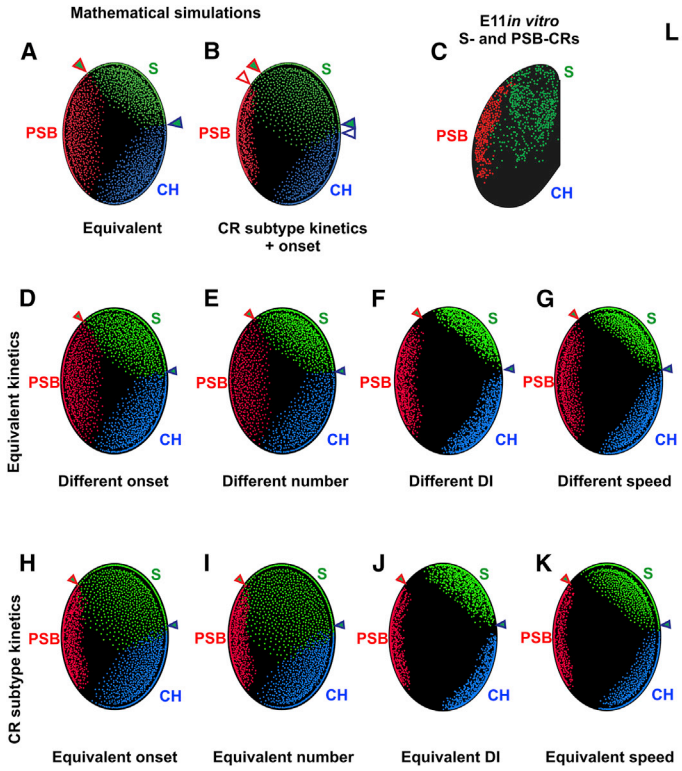

L

Panel	Onset	Mean speed (μm/hr)	DI	Supply from progenitor domain (Total cell number)
A	=	20	0.51	S-CRs: 720 PSB-CRs: 720 CH-CRs: 720
B	≠	S-CRs: 28.0 PSB-CRs: 13.5 CH-CRs: 18.7	0.67 0.31 0.54	S-CRs: 720 PSB-CRs: 540 CH-CRs: 540
D	≠	20	0.51	S-CRs: 720 PSB-CRs: 720 CH-CRs: 720
E	=	20	0.51	S-CRs: 720 PSB-CRs: 540 CH-CRs: 540
F	=	20	0.255	S-CRs: 720 PSB-CRs: 720 CH-CRs: 720
G	=	10	0.51	S-CRs: 720 PSB-CRs: 720 CH-CRs: 720
H	=	S-CRs: 28.0 PSB-CRs: 13.5 CH-CRs: 18.7	0.67 0.31 0.54	S-CRs: 720 PSB-CRs: 720 CH-CRs: 720
I	≠	S-CRs: 28.0 PSB-CRs: 13.5 CH-CRs: 18.7	0.67 0.31 0.54	S-CRs: 720 PSB-CRs: 720 CH-CRs: 720
J	≠	S-CRs: 28.0 PSB-CRs: 13.5 CH-CRs: 18.7	0.255 0.255 0.255	S-CRs: 720 PSB-CRs: 540 CH-CRs: 540
K	≠	S-CRs: 10 PSB-CRs: 10 CH-CRs: 10	0.67 0.31 0.54	S-CRs: 720 PSB-CRs: 540 CH-CRs: 540

Figure 2. Mathematical Simulations Support the Requirement of CR Subtype-Specific Kinetics of Migration and, in Particular, Speed, to Recapitulate Their Specific Repartition In Vivo

(A and B) Final time frame of mathematical simulations of CR subtypes migrating with equivalent (A) and subtype-specific kinetics (B), corresponding to 24 hr and ~E11.0 in vivo (E10 + 24 hr) (S-CRs, green ○; PSB-CRs, red ○; CH-CRs, blue ○). Green arrowheads outlined in red and blue indicate the rostro-lateral and medial territories where S-CRs/PSB-CRs and S-CRs/CH-CRs come into contact at their migration fronts, respectively. White arrowheads outlined in red and blue indicate shift in regions occupied by S-CRs.

(C) Distribution of Dbx1-derived S-CRs (green ○) and PSB-CRs (red ○) quantified in E11 flattened cortical preparations.

(D–K) Last time frame of simulations of CR subtype migration (S-CRs, green ○; PSB-CRs, red ○; CH-CRs, blue ○).

(A, B, and D–K) Simulations generated using equivalent migration kinetics (A and D–G) and subtype-specific migration kinetics (B and H–K) with equivalent (A and E–H) or different onset of migration 6 hr earlier for S-CRs relative to PSB-CRs and CH-CRs (B, D, and I–K), equivalent (A, D, and F–I), or subtype-specific total number of CRs supplied from each progenitor domain (B, E, J, and K), equivalent (A, D–G, and K), or subtype-specific speed of migration (B and H–J), equivalent (A, D–G, and J), or subtype-specific directionality index (DI) (B, H, I, and K).

(L) Parameters used for mathematical simulations. Homotypic weighting coefficients and number of supplied cells from progenitor domains are indicated (see also the Supplemental Experimental Procedures).

kinetics, and, notably, S-CRs are the first to initiate their migration and migrate faster and along more linear trajectories than other subtypes.

To assess how differences in migration of CR subtypes may impact their distribution in cortical territories, we used mathematical modeling. Specifically, cell migration was modeled by the weighted sum of two components: (1) random walking (RW) and (2) contact repulsion (C-Rep) between cells, as recently reported [27]. Both weighting coefficients were numerically determined so as to reproduce the experimental parameter values for the mean speed and DI of each subtype at E10 (Supplemental Experimental Procedures). A simulation where onset and speed of migration (20 μm/hr) were equivalent for all CR subtypes, as previously suggested [27], resulted in equivalent surface area occupancy of the cortex for each subtype (Figures 2A and 2L; Movie S3, left panel). In contrast, simulations introducing our experimentally observed migration kinetics, including onset, speed, and persistence in directionality (Figures 2B and 2L; Movie S3, right panel), remarkably recapitulated the distribution of CR subtypes observed in vitro (Figure 2C) and in vivo [25] at E11. We further tested how each individual migration parameter influenced CR subtypes distribution in both equivalent and CR subtype-specific kinetics mathematical models. We found that changing exclusively the onset of migration for S-CRs (Figures 2A and 2D) or the number of cells produced by each source (Figures 2A and 2E) did not significantly alter their final repartitioning in cortical territories. Similarly, when differences in onset or number of cells were removed from the model with CR subtype-specific kinetics (Figures 2B, 2H, and 2I), no significant changes were observed. However, when either DI or speed were individually decreased by 2-fold in simulations of equivalent (Figures 2F and 2G) or subtype-specific kinetics (Figures 2J and 2K) CR distribution was clearly altered, indicating that speed and directionality of migration appear to be the primary parameters regulating CRs distribution. Thus, the simulations predict that experimentally observed

differences in migration kinetics of CR subtypes, rather than onset and number of CRs produced at each progenitor domain, are required and sufficient to determine their specific repartition in early cortical territories in vivo.

These results were surprising given that CRs were previously shown to migrate by a common mechanism of contact-mediated repulsion with equivalent speeds and low persistence in directionality on 2D substrates in vitro [27]. We thus studied the migratory behavior of S-CRs and CH-CRs upon cell-cell contact in flattened cortical preparations at E10 and E11 using time-lapse microscopy. We scored three behaviors likely resulting from distinct cellular mechanisms: (1) contact repulsion, (2) contact deviation, and (3) contact steering (Movie S4). At both stages, the most prevalent behavior observed for S-CRs and CH-CR subtypes was contact deviation (Figures S1L–S1N and S1P) with contact repulsion accounting for only a small percentage of behaviors. No significant differences in response to contact were observed between CR subtypes over time although between E10 and E11 S-CRs and CH-CRs differed with respect to speed and directionality. In addition, convergence of migrating CRs was observed at specific rostro-medial levels (Figure S1O; Movie S4). Together, these results suggest that subtype-specific and temporal differences in speed and directionality do not correlate with differences in their contact-repulsive interactions and points to the existence of additional mechanisms regulating these migration parameters.

VAMP3-Dependent Vesicle Trafficking Controls CR Speed of Migration and Redistribution in a Cell-Autonomous Manner

To elucidate the molecular mechanisms underlying CR subtypes differences in migration, we screened a previously reported transcriptomic dataset obtained from FACS-purified S-CRs and PSB-CRs [25]. Surprisingly, vesicle-associated membrane protein 3 (VAMP3), a member of the VAMP1–3 subfamily of recycling endosomal vesicular SNAREs (*N*-ethylmaleimide-sensitive factor attachment protein receptor) [28], which was previously shown to be exclusively expressed in non-neuronal cells in the mature brain [29], was highly expressed in CR cells compared to other VAMPs (Figure S2A). Via its interaction with plasma membrane SNAREs, VAMP3 plays an essential role in the exocytosis of recycling endosomes [30] and promotes the motility of epithelial cells and macrophages through integrin receptor recycling [31–35], raising the possibility that VAMP3 may regulate CR migration. Using VAMP3 immunostaining on E11.5 $Dbx1^{YFP}$ telencephalons, we confirmed the presence of VAMP3-positive vesicles in $YFP^{+}Reln^{+}$ (Reelin) S-CRs, including in their leading process (inset), and in $YFP^{-}Reln^{+}$ CH-CRs (Figure 3A, green and blue arrows, respectively). The microarrays further suggested that S-CRs (DM) expressed VAMP3 at higher levels relative to PSB-CRs (DL), with PSB-CRs reciprocally showing greater enrichment in VAMP2. VAMP2 is best known for mediating neurotransmitter release in the adult nervous system [36]. However, during development, it mediates axon-guidance through the trafficking of Neuropilin1 and PlexinA1 receptors [37], and by asymmetric membrane transport and exocytosis [38], both mechanisms that could underlie the chemotaxis of migrating cells. We therefore quantified the percentage of CR subtypes expressing VAMP2 and VAMP3 in E11 $Dbx1^{YFP}$ and $p73^{YFP}$ cortical regions close to their sources using immunohistochemistry for Reln and Calretinin (Calr) so as to discriminate between the three subtypes (see the Supplemental Experimental Procedures). Counts showed that 88% and 95% of $Dbx1^{YFP+}Reln^{+}$ S-CRs and $Dbx1^{YFP-}Reln^{+}$ CH-CRs, respectively, express VAMP3, in contrast to only 50% of $Dbx1^{YFP+}Reln^{+}$ PSB-CRs (Figure S2B). In addition, 83% of $p73^{YFP-}Calr^{+}$ PSB-CRs expressed VAMP2, compared with only 13% of $p73^{YFP+}$ S-CRs and 19% of $p73^{YFP+}Calr^{+}$ CH-CRs. Further, quantification of the signal intensity of VAMP3 and VAMP2 immunostaining showed significantly higher expression of VAMP3 in S-CRs and CH-CRs relative to PSB-CRs, with PSB-CRs expressing VAMP2 most strongly (Figure S2C), which was consistent with our counts and microarray data. Thus, these data confirm differential expression of VAMP2 and VAMP3 proteins in subsets of migrating CRs and raises the question of their function.

To assess the role of VAMP2 and VAMP3 in CRs migration, we took advantage of the *iBot* transgenic mouse line that allows for Cre recombinase-dependent expression of the light chain of clostridial botulinum neurotoxin B (BoNT/B) (*CAGboNT/B,EGFP*) [39]. This toxin selectively cleaves and inactivates VAMP1–3, which have reported redundant functions [29]. We crossed the *iBot* line with $p73^{Cre}$ mice to specifically target S-CRs (S-*iBot*) and CH-CRs (CH-*iBot*) and allow the simultaneous imaging of their migration. Imaging of E11 $p73^{Cre}$;*iBot* flattened cortices showed a significant increase in CRs mean speed of migration along the entire medial axis relative to control explants (Figures 3B–3H; Movie S5) without changes in their directionality index. These results demonstrate that VAMP1–3-dependent vesicular trafficking, likely the most highly expressed VAMP3, specifically regulates the speed of migration of S-CRs and CH-CRs in a cell-autonomous manner. It also suggests that directionality and speed of migration are controlled by distinct molecular pathways.

To study how faster migration speed of S-*iBot* and CH-*iBot* CRs impacts their distribution in the embryonic cortex, we generated mathematical simulations using data obtained from our live-imaging experiments and analyzed the distribution of CR cells in vivo. Simulations predicted a precocious invasion of S-*iBot* and CH-*iBot* in the dorsal cortex (Figure 3I, dashed area; Movie S5) and increased mixing of CR subtypes in the rostro-lateral and caudo-dorsal regions (Figure 3I). We next analyzed the in vivo distribution of CR subtypes using immunohistochemistry for Reln and Calr (goat antibodies (Swant)) [23], which allows to discriminate S-CRs ($Reln^{+}Calr^{-}$) from both PSB-CRs and CH-CRs ($Reln^{+}Calr^{+}$), and for GFP, which allows to label both S-CRs and CH-CRs (Figures 4A–4G and S3). We found an ectopic accumulation of CH-CRs ($GFP^{+}Reln^{+}Calr^{+}$) in the rostro-dorsal cortex, and, consistent with the simulations, of S-CRs ($GFP^{+}Reln^{+}Calr^{-}$) in the caudo-dorsal cortex in *iBot* mutants. No changes in the total number of $Reln^{+}$ cells were observed, indicating that CRs were correctly generated and specified. The ectopic accumulation of CH-CRs and S-CRs in the dorsal cortex at rostral and caudal levels, respectively, in *iBot* embryos was consistent with their increased speed of migration observed by time-lapse imaging resulting in their invasion and accumulation in more distant territories (blue and green arrows in Figure 4H). This also led to a change in the relative number of S-CRs and CH-CRs in the caudal cortex (green and

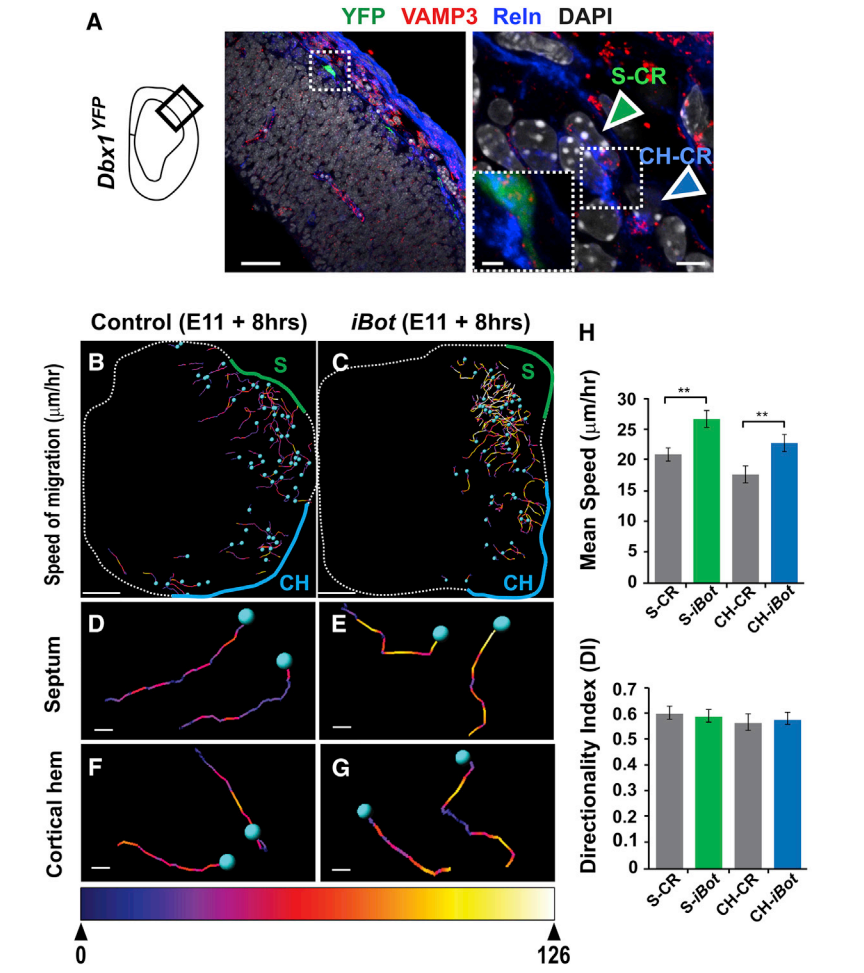

Figure 3. CRs Express VAMP3 and Cleavage of Vamp1–3 Increases Their Speed of Migration in a Cell-Autonomous Manner

(A) Confocal images of the dorso-lateral cortex from E11.5 *Dbx1*^{YFP} embryos immunostained for VAMP3 (red), Reln (blue), GFP (green), and nuclear counterstain with DAPI (gray). High magnification (right) shows VAMP3 vesicular-like staining in migrating Dbx1-derived YFP^{+}Reln^{+} CRs (green arrow) and YFP^{-}Reln^{+} CH-CRs (blue arrow). Inset is a high magnification of the leading process enriched in VAMP3. VAMP3 staining is also observed in cells surrounding CRs and meninges.

(B–G) Cell tracks from 8-hr live imaging of S-CRs and CH-CRs in flattened cortices of *p73*^{YFP} control and BoNT/B-expressing *p73;iBot* at E11. Tracks are color coded for speed (high magnification of representative cell tracks in D–G).

(H) Mean speed of migration and DI of S-CRs and CH-CRs in control (gray) and *p73;iBot* (green and blue columns, respectively). S-CRs (n = 134 cells), S-*iBot* (n = 129 cells); CH-CRs (n = 81 cells), CH-*iBot* (n = 77 cells for mean speed and n = 75 cells for DI). Values: mean ± SEM; two-tailed unpaired t test **p < 0.01.

(I) Final time frame of mathematical simulations generated from experimental data of tracked CRs in E11 control (*p73*^{YFP}) and mutant embryos (*p73;iBot*) showing predicted repartition of S-CR (green ○), PSB-CR (red ○), and CH-CR (blue ○). Green arrowheads outlined in red and blue indicate where S-CRs/PSB-CRs and S-CRs/CH-CRs come into contact at their migration fronts, respectively, in the rostro-lateral and medial territories (shown at high magnification in the right-hand images). White arrowheads outlined in red and blue show shift in regional occupancy of S-CRs in *iBot* mutants.

Scale bars, 50 μm (A, left); 5 μm (A, right); 2.5 μm (right, inset); 200 μm (B and C); 30 μm (D–G). See also Figure S2.

blue ○ in Figure 4H), as predicted by the simulation (Figure 3I). Furthermore, an ectopic accumulation of PSB-CRs (GFP^{-}Reln^{+} Calr^{+}) was observed in the dorsal and lateral cortex (Figures 4H and S3) at rostral levels, showing a non-cell autonomous rostro-medial redistribution of PSB-CRs in *iBot* mutants (red arrows in Figure 4H), likely preventing S-CRs from invading the rostral dorso-lateral cortex. Analysis of the distribution of GFP^{+} p73-derived CRs (S-CRs and CH-CRs) in *iBot* mutants at E17.5 showed their increased accumulation in the dorsal cortex at rostral levels, with no changes in their total number, consistent with their enhanced dispersion resulting from their faster migration speeds at earlier stages (Figures S3F–S3H). As VAMP3 was the most highly expressed member in S-CRs and CH-CRs, we further assessed whether it was specifically involved in CRs migration by analyzing the distribution of CR subtypes in *Vamp3* mutant embryos (Figure S3I). We found that VAMP3 inactivation altered the distribution of CR subtypes, but not the total number of Reln^{+} cells, in the dorsal and lateral cortex indicating that the cell-autonomous activity of VAMPs in CR cell migration likely involves VAMP3. Together, these results show that cell-autonomous inactivation of VAMP3 in S-CRs and CH-CRs increases their migration speed resulting in their redistribution to more distant locations and enhances mixing of CR subtypes specifically in the dorso-lateral cortex at rostral levels and the dorsal cortex at mid-caudal levels in vivo.

VAMP3 Controls the Size of Higher-Order Areas in the Postnatal Cerebral Cortex

We have previously shown that loss of S-CRs influence the early regionalization of the cerebral cortex and the size of the primary motor cortex [22]. To investigate whether changes in CRs'

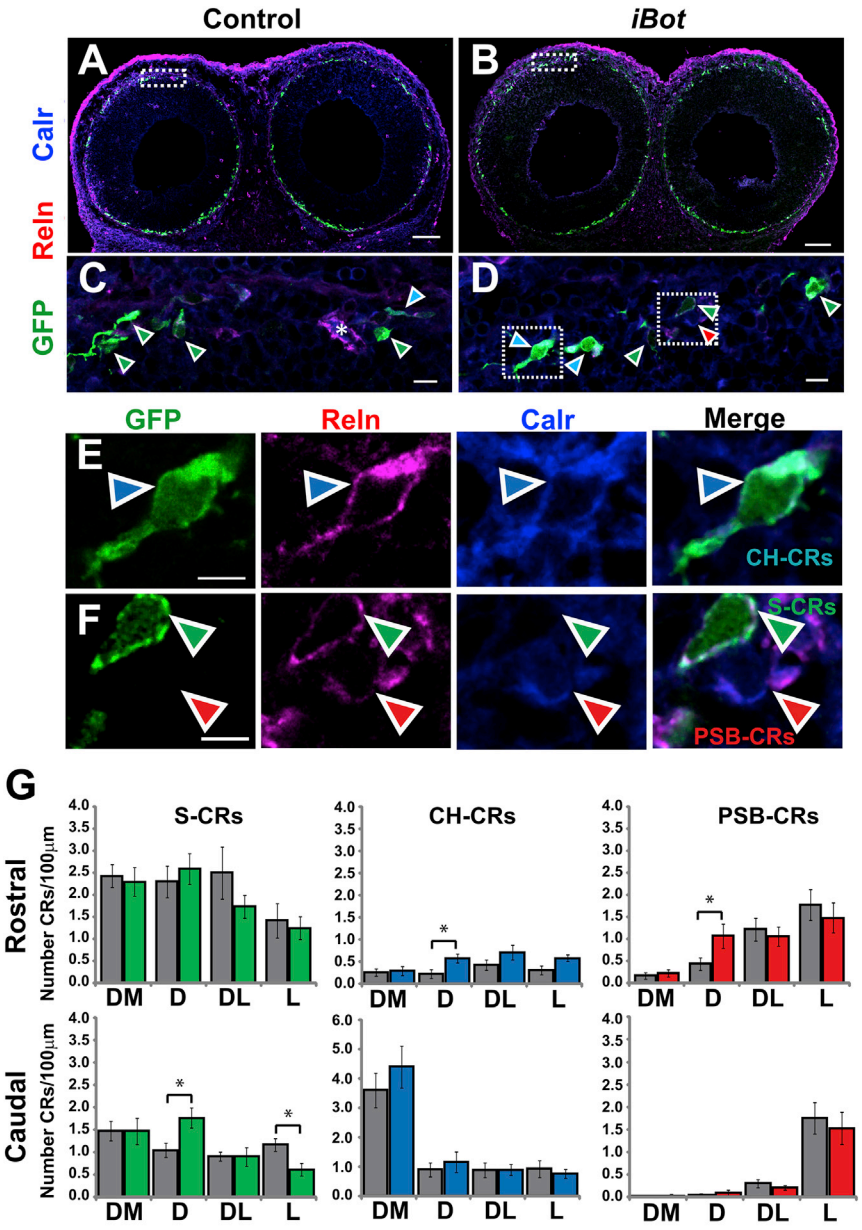

Figure 4. Redistribution of CR Subtypes in the Developing Cerebral Cortex of *iBot* Mutants at E11

(A–F) Confocal images of coronal sections through the rostral telencephalon from E11 control $p73^{YFP}$ and *p73;iBot* embryos immunostained for GFP (green), Reln (red), and Calr (blue). (C and D) High magnifications of the dorsal pallium corresponding to boxed regions in (A) and (B). Asterisk denotes blood vessel. (E and F) High magnifications of boxed regions in (C) and (D). Molecular characterization of S-CRs (GFP^+Reln^+, green arrowheads), CH-CRs ($GFP^+Reln^+gCalr^+$, blue arrowheads), and PSB-CRs ($Reln^+gCalr^+$, red arrowheads) used for quantification in (G).

(G) Quantifications at rostral (L1 in Figure S3) and caudal levels (L4 in Figure S3) along the rostral-caudal axis of the telencephalon. Gray and colored columns show counts in control (Ctrl) and *p73;iBot* mutants, respectively: S-CRs (GFP^+Reln^+, green), CH-CRs ($GFP^+Reln^+gCalr^+$ and single GFP^+ [later born CH-CRs with delayed expression of Reln and Calr, blue]), PSB-CRs ($GFP^-Reln^+gCalr^+$, red). DM, dorsal-medial; D, dorsal; DL, dorsal-lateral; L, lateral (see also Figure S3 for subdivisions along the medial-lateral axis). Graphical representation of normalized cell counts (cells/100 μm ± SEM) (n = 3 brains for each genotype). Student's t test; $^*p \leq 0.05$.

(H) Schema summarizing the distribution and inferred migration pathways of CR subtypes along the rostro-caudal axis in E11 controls and *iBot* mutant telencephalons. Quantifications of CR subtypes (Figure S3) suggested that faster migrating CH-CRs preferentially follow a lateral route to redistribute in rostral territories in *iBot* mutants (blue arrows). High magnifications of yellow and brown boxes highlight the distribution in rostro-lateral and caudo-medial territories, respectively. Double-headed arrows indicate faster migrating CRs.

Scale bars, 100 μm (A and B), 10 μm (C and D), and 5 μm (E and F). See also Figure S3.

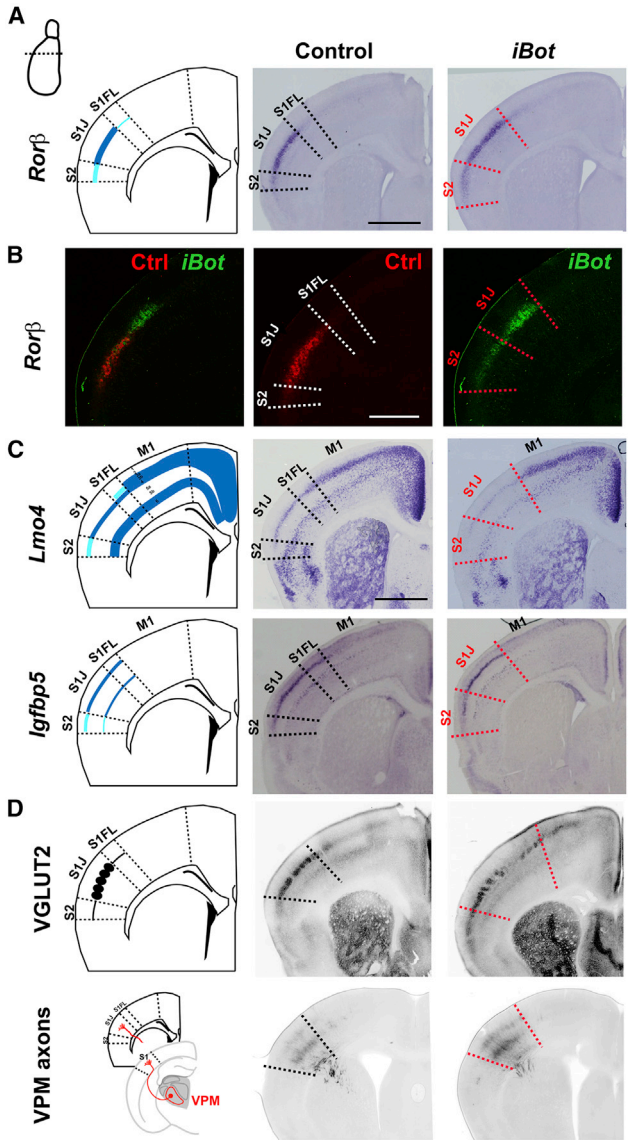

Figure 5. VAMP1–3 Regulates the Position, Size, and Connectivity of Rostro-lateral Cortical Areas

(A–C) In situ hybridization on coronal sections of P8 control and *p73;iBot* mutant brains using mRNA probes for *Rorβ* (n = 3) (A and B), *Lmo4* (n = 5), and *Igfbp5* (n = 3) (C) at rostral levels. (A) shows a dorsal displacement of S1J at the expense of S1FL and an enlargement of S2. (B) *Rorβ* mRNA localization shown in artificial colors for control (red) and *iBot* mutant (green) brains. The left-hand panel shows merged false-color images highlighting the dorsal shift of S1J in mutants. (C) shows the M1/S1 border, demarcated by *Igfbp5* staining of S1, is not altered.

(D) Immunohistochemistry for VGLUT2 and anterograde labeling of thalamocortical axons from the VPM on coronal sections of P8 control and *p73;iBot* mutant at rostral levels showing re-targeting of afferents to the dorsally displaced S1J.

Cartoons in (A) and (C) display the layer-specific molecular code for each area and in (D) the projections from the VPM thalamic nucleus. Dashed lines delimit each cortical area in controls (black) and changes in mutants (red). Low expression levels, light blue; high levels, dark blue. S1J, primary somatosensory cortex jaw region; S1FL, primary somatosensory cortex forelimb region; S2, secondary somatosensory cortex; M1, primary motor cortex; VPM, ventral posterior medial nucleus. Scale bars, 500 μm (A–C and apply to all other panels). See also Figures S4 and S5.

distribution alter cortical patterning, we first assessed whether the regionalization of the cortex was altered in E11.5 $p73^{Cre}$;*iBot* and control brains by in situ hybridization. This showed no changes in the expression of genes that specify rostral (*Fgf8)* and caudal (*Wnt3a)* signaling centers or in *Pax6*, *Sp8*, *Emx2*, and *COUP-TF1* corresponding to transcription factors whose graded expression is involved in early cortical regionalization (Figure S4) [3]. Moreover, we found the regionalized expression of *Wnt8b* and *Fgf17*, which, respectively, delineate the medial and rostral subdivisions of the cortex [40, 41] were comparable in $p73^{Cre}$;*iBot* and control brains. Together, these results show that inactivation of VAMP2 and VAMP3 in S-CRs and CH-CRs does not alter signaling centers or early cortical patterning. We next examined area formation in $p73^{Cre}$;*iBot* brains at postnatal day 8 (P8) by in situ hybridization on coronal sections using area and layer-specific markers *Rorβ*, *Lmo4*, and *Igfbp5* (Figures 5, 6, and S5). No changes in the border between S1 and primary motor cortex (M1) were detected, as shown by the extent of high *Igfbp5* and *Lmo4* expression (labeling S1 and M1, respectively, at this level) (Figure 5C). Intriguingly, however, we detected changes in subregions of S1 at rostral levels, namely, the replacement of somatosensory forelimb fields (S1FL) by somatosensory jaw territories (S1J) (as labeled by low *Rorβ* expression in layer 4 of S1FL and high of S1J) in *iBot* mutants compared to controls (Figures 5A, 5B, 6C, and S5A), although the overall size of S1 was unchanged. This was associated with an enlargement of secondary somatosensory cortex (S2) (low *Rorβ*, *Lmo4*, and *Igfbp5* expression). Notably, immunocytochemistry against VGLUT2, which is expressed specifically by the presynaptic terminals of thalamocortical synapses [5] and anterograde labeling of thalamo-cortical axons from the ventral posterior medial (VPM) nucleus, which conveys input from the snout and jaw, also showed a dorsal shift of layer 4 afferents (Figure 5D) and confirmed a re-routing of sensory connections. Furthermore, at mid-caudal levels medial visual secondary cortex (V2ML/MM) was replaced by parietal association cortex (LPtA/MPtA) as shown by *Lmo4* mRNA expression restricted to layers 4 and 6 and low levels of *Rorβ* in layer 4 characteristic of LPtA/MPtA in *iBot* mutants compared to controls (V2ML/MM expressing *Lmo4* in layers 3, 5, and 6 and no *Rorβ*) (Figures 6A and 6C). Analysis along the entire rostro-caudal axis indicated a 400-μm caudal expansion of parietal association cortex at the expense of visual secondary areas (Figure S5B). An increase in the size of primary somatosensory (S1)/parietal posterior association (PtPR/PtPD) (S1/PtP) cortex and a reduction of auditory secondary areas (AuD) were also observed at this level. Similar phenotypes were detected in *Vamp3* mutants. In particular, V2ML/MM was replaced by LPtA/MPtA, S1/PtP was increased at the expense of AuD (Figure S6A), and the lateral visual secondary cortex (V2L) was replaced by visual primary cortex (V1) (Figures 6B, 6C, and S6A). In contrast, no differences in the size of S1 and S2 areas were detected at rostral levels in *Vamp3* mutants (Figure S6B). Thus, VAMP3 inactivation results in the expansion of parietal association cortex and V1 at the expense of visual and auditory secondary areas. Collectively, our data indicate that recycling endosomal VAMPs, most likely primarily VAMP3, modulate the speed of S-CRs and CH-CRs migration in a cell-autonomous manner and their redistribution in embryonic cortical territories. It further shows that CR repartition is involved

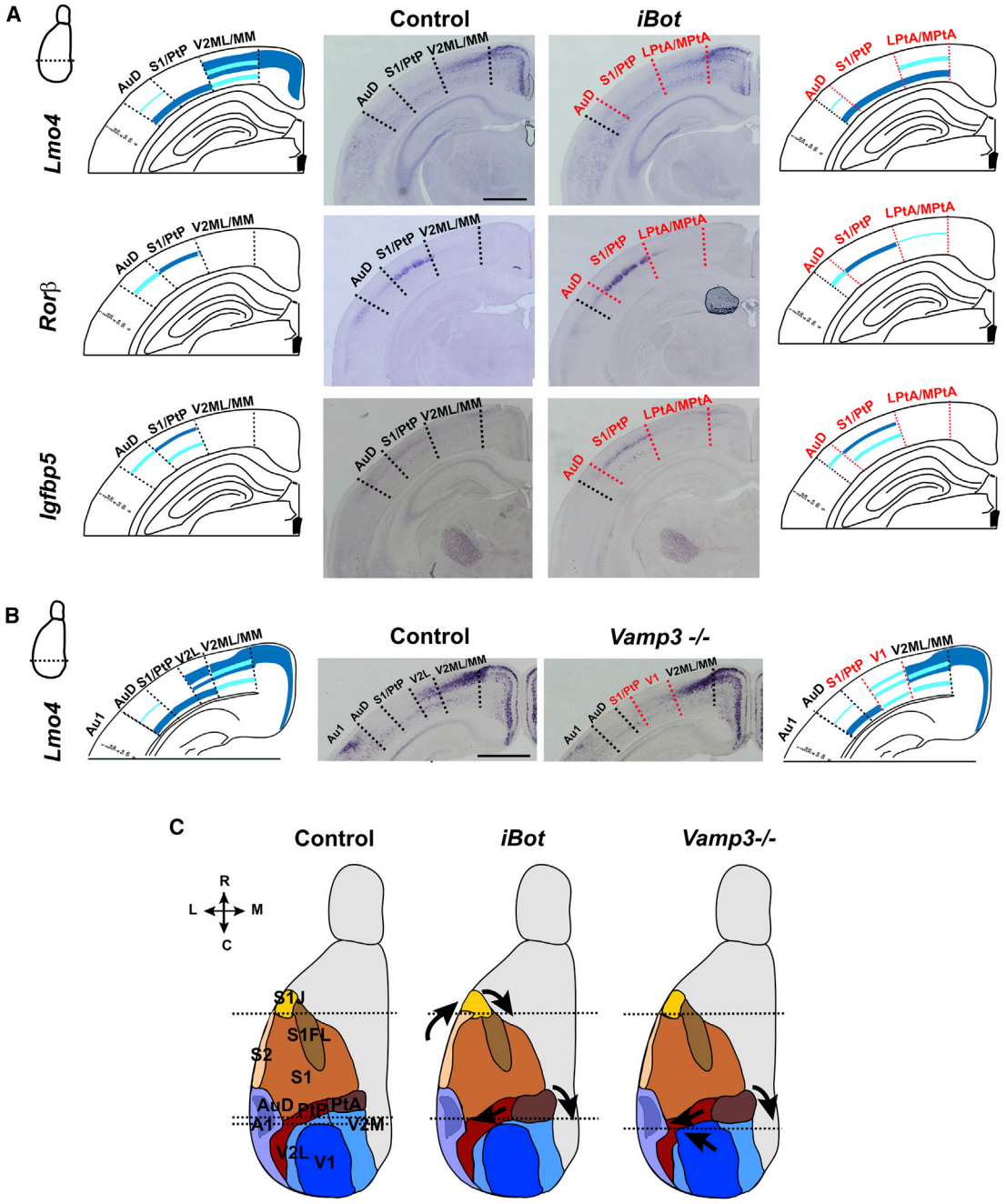

Figure 6. VAMP3 Regulates the Size of Higher-Order Cortical Areas in the Caudal Neocortex

(A) In situ hybridization on coronal sections of P8 control and *p73;iBot* mutant brains using mRNA probes for *Lmo4* (n = 5), *Rorβ* (n = 3), and *Igfbp5* (n = 3) at mid-caudal levels showing a replacement of V2ML/MM by LPtA/MPtA and an enlargement of S1/PtP at the expense of AuD.

(B) In situ hybridization on coronal sections of P8 *Vamp3*$^{+/-}$ (control) and *Vamp3*$^{-/-}$ mutant brains at caudal levels using an *Lmo4* mRNA probe showing V2L is replaced by V1 (n = 3 for each genotype).

(C) Cartoon of arealization defects in *iBot* and *Vamp3* mutant brains. Dashed lines show levels along the anterior-posterior axis corresponding to coronal sections in (A) and (B) and Figure 5 for rostral levels.

Cartoons in (A) and (B) display the layer-specific molecular code for each area. Dashed lines delimit each cortical area in controls (black) and changes in mutants (red). Low expression levels, light blue; high levels, dark blue. S1J, primary somatosensory cortex jaw region; S1FL, primary somatosensory cortex forelimb region; S2, secondary somatosensory cortex; M1, primary motor cortex; V2ML/MM (V2M in C), secondary visual cortex mediolateral/mediomedial; LPtA/MPtA (PtA in C), lateral parietal association/medial parietal association cortex; S1/PtP (PtP in C), primary somatosensory/parietal association cortex posterior rostral and dorsal; AuD, auditory secondary cortex dorsal (AuD). Scale bars, 1 mm (A and B). See also Figure S6.

in controlling the size of higher-order areas in the postnatal cerebral cortex and somatotopic targeting of sensory afferents from the thalamus (Figure S6C), without affecting signaling centers.

DISCUSSION

Our findings reveal that in the cerebral cortex, the migration kinetics of early-born signaling neurons regulates the size of higher-order areas, whose expansion is a hallmark of cortical evolution. We show that speed of migration is controlled cell-autonomously in CR subtypes by VAMP3-dependent vesicular trafficking mechanisms, which determines their distribution and, likely, their spatial-temporal signaling activities in cortical territories, to ultimately influence the size and connectivity of higher-order cortical areas. Mechanistically, our results demonstrate for the first time a role for VAMP3 in postmitotic neurons (CRs) and in early brain development. Previously, this v-SNARE was thought to be expressed exclusively in non-neuronal cells in the mature brain and was considered to have a redundant role with VAMP1 and VAMP2 when expressed in the same cells [29, 42]. Our observations reveal a key role for this v-SNARE in modulating the migration speed of an important neuronal population during cortical development and in regulating the size and wiring of higher-order areas in the auditory, visual, and somatosensory systems.

Mechanisms of CR Migration and Vesicular Trafficking

Our results show that the specific repartition of CR subtypes in the developing cortex is crucial for cortical wiring. This repartition is determined by subtype-specific migration kinetics and, in particular, speed and directionality. Several molecular pathways have been recently shown to regulate CR migration, namely, Ebf2/3, Cxcl12/Cxcr4, Eph/Ephrins, and Sema3E/PlexinD1 [27, 43–45]. However, these studies focused on migration from the cortical hem and little was known regarding the migration of CRs from other sources. Indeed, it was suggested that common mechanisms govern the movement of all subtypes on a 2D substrate in vitro [27]. Here, we reveal a more complex regulatory mechanism in which CR subtypes differ in their onset, kinetics, and direction of migration. Using mathematical models, we predict that differences in migration speed and DI are primary parameters that regulate CR subtypes differential invasion and occupancy of cortical territories. We confirm these predictions by identifying a novel VAMP3-dependent mechanism that cell-autonomously modulates the migration speed of two CR subtypes, S-CRs and CH-CRs, and show that impairing VAMP3 activity increases their migration speed and dispersion thereby altering the composition of CRs in specific cortical territories in vivo. Contact repulsion was previously shown to be a mechanism by which CRs disperse and reciprocally prevent their invasion of adjacent cortical territories [23, 25, 27, 44]. Notably, abrogation of Ephrin/Eph signaling indicated that, while this perturbed contact-repulsive interactions between CRs and increased their directionality index in vitro, it did not affect their migration speed and general motility [27]. We reciprocally show that impairing VAMP3 activity in migrating CRs resulted in faster migration speeds but did not alter their directionality index. Moreover, we observed no significant differences in migratory behavior in response to contact between CR subtypes or overtime although they differed with respect to speed and directionality. Together, these results suggest that directionality and speed of migration are independently controlled by two distinct molecular pathways, likely involving Ephrin/Eph-mediated contact repulsion and VAMP3-mediated vesicular traffic, respectively.

Our data identify a novel molecular pathway that negatively modulates CRs migration speed. Recently, Sema3E/PlexinD1 was shown to decrease CH-CRs motility by negatively modulating ADF/Cofilin signaling downstream of PlexinD1, the former being required to initiate actin polymerization and thus regulate leading process morphology and chemotaxis [45]. Similar to *Vamp3* and *iBot* mutants, an increased dispersion of CH-CRs to more distant cortical territories was reported in *PlexinD1*-null mice in vivo. Notably, VAMP2-dependent vesicular trafficking of PlexinA1/Neuropilin1 receptors has been shown to underlie Sema3A-dependent repulsion during axon guidance [37]. This raises the possibility that defects in VAMP3-dependent recycling of PlexinD1 receptors could impair CH-CRs response to Sema3E and mediate the faster migration speed and redistribution in *Vamp3* and *iBot* mutants.

Our data indicate that VAMP3 is the most important of the VAMP1–3 subfamily of recycling endosome members implicated in this process based on transcriptomics data, immunohistochemical analysis, and the similar cortical phenotype of *iBot* mutants with abrogation of VAMPs1–3 specifically in CRs and *Vamp3* mutants with a ubiquitous invalidation of the gene. Moreover, we find CR subtypes differentially express VAMP proteins with S-CRs and CH-CRs enriched in VAMP3 and PSB-CRs in VAMP2, which could underlie their distinct behaviors. VAMP2 has been shown to regulate axonal repulsion and growth cone attraction by asymmetric membrane trafficking and exocytosis [38, 46]. Growth cone steering in navigating axons and in the leading process of migrating neurons share common mechanisms, with the former suggested to result from an imbalance of localized exocytosis and endocytosis [46]. It remains to be shown whether VAMP2 and VAMP3 differentially regulate endocytosis and exocytosis at leading edge of migrating CR subtypes and give rise to differences in their motility and directionality.

A role for polarized exocytosis has also been shown to underlie autocrine modes of migration through the secretion of chemokinetic gradients, which promote cell motility [47]. Interestingly, inactivation of VAMP3 in epithelial cells has been reported to inhibit migration and integrin trafficking in cultured cells [31] rather than promoting it, suggesting that VAMP3 may regulate the motility of CRs by different mechanisms or that the context of brain slices and developing brains in situ (this study) may differ from in vitro cultures, the latter of which has been shown to favor amoeboid migration [48]. Notably, autocrine stimulation of cell motility through the secretion of EGF modulates migration speed more efficiently than exogenous stimulation [49]. While the molecular partners underlying this mechanism remain to be fully explored, our results further suggest that VAMP3-recycling endosomes may secrete molecules regulating CR migration. Among possible VAMP3-dependent CR secreted molecules, Reelin appears as a good candidate given its established role in the radial migration of glutamatergic neurons [50], the dispersal of progenitors in the rostral migratory stream [51], and the migration of epithelial cells [52]. Recently, the *Drosophila*

ER/Golgi SNARE member Ykt6 was shown to mediate the trafficking of Wnt morphogens through endosomal compartments and their secretion in exosomes [53]. Given that CRs are also enriched in morphogens [25], it is possible that VAMP3-dependent secretion of several molecules including Reelin and morphogens by CR cells may generate an autocrine feedback loop to control their speed and, therefore, their signaling activity in a spatiotemporal manner. This autocrine feedback loop would operate as an intrinsic speed rheostat for CR migration. The simultaneous coupling of CRs motility with potential morphogen secretion would exert a strict spatiotemporal regulation of CRs' signaling activities in cortical territories.

CRs Distribution and Cortical Area Patterning

We have previously shown that CRs are enriched in morphogens and that the ablation of S-CRs between E10.5 and E11.5 results in an invasion of the depleted territories by the other CR subtypes by E12.5 [25]. This influences early patterning gradients of transcription factors and the position and size of the primary motor cortex. Here, we show that impairing VAMP1–3 activity increases S-CRs and CH-CRs migration speed and results in their ectopic redistribution in more distant territories thereby altering the composition of CRs in specific cortical territories in vivo. In particular, CR subtypes specifically redistribute in the dorso-lateral and dorsal cortex at rostral and caudal levels, respectively, without changes in the total number of CRs in the cortex. Intriguingly, this leads to non-cell-autonomous changes in the size of higher-order cortical areas in the somatosensory, auditory, and visual cortices, without altering that of territories allocated to primary cortical function and in the absence of defects in signaling centers or early cortical patterning. Recently, the size of primary cortical areas has also been reported to be altered in hem-ablated mutants, which present a total loss of hem-derived CRs in addition to the cortical hem itself [54]. Together, these results suggest that the total number of CRs is crucial in controlling the size of primary cortical areas, whereas the specific redistribution of CR subtypes in the absence of CR loss is involved in regulating the size of areas that form at regions interspersed between primary areas, namely, secondary and associative territories.

Our mathematical simulations highlight how small changes in migration kinetics affect the distribution of CRs in specific embryonic territories. In addition to an ectopic invasion of the dorsal cortex, these predict a change in composition and increased mixing in the dorso-lateral and dorso-medial cortex at rostral and mid-caudal levels, respectively. These territories are located where gradients of expression of transcription factors, involved in early cortical regionalization [3], are at their lowest levels and specifically at the intersection of opposing patterning gradients. These embryonic territories may correspond to regions interspersed between primary areas in the adult animal where secondary and association areas form and that are of foremost importance for higher level processing in primates and humans. Our time-lapse studies show that the first streams of CRs leaving the progenitor domains at E10 stop migrating when reaching the dorsal cortex while subsequent streams continue migrating from these sources and bypass the previously positioned CRs to fill up available space. Our analysis of *iBot* mutants at E17.5 also show that CRs preferential distributions are still observed at late stages of development. These results strongly argue that the first streams of CRs are anchored to specific cortical territories and that their preferential distributions are established and, at least in part, maintained from the earliest stages of corticogenesis. Consistent with this, it has been shown that CRs are misplaced in layer 1 in the absence of radial glia [55] suggesting that this interaction is involved in maintaining the position and distribution of CRs. This would ensure a temporal and spatial control of their signaling activity and a stable point-to-point link between early cortical regions and areal borders at later stages. Our work, thus, suggests a novel mechanism by which signaling through a precise composition of CR subtypes is required to pre-pattern higher-order cortical territories by delineating the size of these territories. In addition, this also influences the targeting of thalamo-cortical axons, which will later refine patterning by experience-driven inputs [4, 5] (Figure S6C). This is consistent with previous reports that showed that the borders of the secondary visual cortex surrounding primary visual area are not influenced by sensory inputs [4] but is within a uniform visual territory that the distinction between primary and secondary areas occurs upon the arrival of thalamo-cortical inputs at postnatal stages [5]. CRs have previously been shown to guide entorhinal-hippocampal axons [15] and to further integrate in early cortical circuits [17], thus raising the possibility that CRs could additionally influence the differentiation of higher-order areas through promoting the maturation of cortical columns. Pre-patterning through VAMP3-mediated secretion regulating migration and distribution of CR subtypes in prospective higher-order cortical territories would, thus, ensure a bifunctional mechanism allowing for robustness of patterning by setting the size of these territories at embryonic stages and plasticity by later refinement driven by sensory experience. Notably, narrow areas both at the occipital-temporal and parietal-temporal borders have been described in rodents, in addition to primates, which contain a mixture of modality-specific neuronal types as well as multisensory neurons [56]. These multisensory populations in these border regions represent a vast proportion of the neurons suggesting that these transitional zones may integrate both cross-modal and multisensory information processing. The territories, whose size we find to be influenced by VAMP3-mediated redistribution of CR subtypes, comprise secondary and association areas of the somatosensory, auditory, and visual systems and are all located at these borders between uni-modal primary areas and are characterized by a mixed cytoarchitecture [57]. This strongly supports the view that they are territories likely responding to cross-modal and/or multisensory inputs. The relative size of cortical territories dedicated to higher-order areas have particularly evolved in humans. Our results open the intriguing possibility that pre-patterning through a tight control of kinetics of migration of signaling CR subtypes might have contributed to the evolution of cortical connectivity.

EXPERIMENTAL PROCEDURES

Ethics Statement

All animals were handled in strict accordance with good animal practice as defined by the national animal welfare bodies, and all mouse work was approved by the Veterinary Services of Paris (authorization number: 75-1454) and approved by the Animal Experimentation Ethical Committee Buffon (CEEA-40) (reference: CEB-34-2012).

Animals

Dbx1^{iresCre} [23, 25] and *DeltaNp73*$^{CreiresEGFP/+}$ [26] were crossed with *ROSA26*$^{loxP\text{-}STOP\text{-}loxP\text{-}YFP}$ reporter line to permanently trace CR subtypes of the *Dbx1* (septum and PSB) and *DeltaNp73* (septum and cortical hem) lineages. Mice in which Botulinum neurotoxin B is expressed upon Cre recombination (*iBot* line; Tg[CAG-boNT/B,-EGFP]U75-56Fwp/J) [39] were crossed with *DeltaNp73*$^{CreiresEGFP/+}$ mice to specifically cleave VAMP 1,2,3 in migrating CR cells. Global inactivation of VAMP3 was analyzed in *Vamp3*-null mice [42].

Whole Flattened Cerebral Cortical Preparations

Flattened whole cerebral cortices were dissected from E10-E12 *Dbx1*$^{Cre/+}$;*ROSA26*$^{YFP/+}$ (*Dbx1*^{YFP}), *DeltaNp73*$^{Cre/+}$;*ROSA26*$^{YFP/+}$ (*p73*^{YFP}), and *DeltaNp73*$^{Cre/+}$;*iBot:GFP* (*p73;iBot*) embryos, ensuring the meninges were preserved and cultured for 4 hr on Millicell (Millipore) permeable membrane inserts in phenol-red-free high glucose DMEM (Sigma) with B27 serum (Gibco) and 100 μg/ml penicillin/streptomycin antibiotics (Sigma) at 37°C with 5% CO_2 prior to live imaging. Immediately before imaging, the flattened cortical explants were transferred with the underlying Millicell membranes and inverted onto a bespoke glass-bottom microscope imaging chamber with the pial surface directly adjacent to the glass, and secured by adding 100 μl of purified bovine collagen (Advanced Biomatrix), which was polymerized at 37°C and 5% CO_2. Inverted confocal microscopy (Leica 710 and Leica 780) was used for live-image acquisition over 4–14 hr at 37°C and 5% CO_2 in a regulated chamber. Time lapses were analyzed with the spot cell-tracking module of Imaris software.

Mathematical Simulations of the Dynamics of CR Cell Distribution

Mathematical simulations were generated according to the experimentally obtained parameters of (1) onset of migration, (2) mean speed of each CR subtype, and (3) persistence in directionality (directionality index [DI]) (see the Supplemental Experimental Procedures). Cell migration was modeled by the weighted sum of two components: (1) random motion (walking) and (2) contact repulsion between cells. Mathematically, it is given by the following stochastic differential equations:

$$dx_i = w_1 dw_x - w_2 \left(\frac{\partial}{\partial x_i} \sum_j U(r_{i,j}) \right) dt \quad (1)$$

$$dy_i = w_1 dw_y - w_2 \left(\frac{\partial}{\partial y_i} \sum_j U(r_{i,j}) \right) dt, \quad (2)$$

where (x_i, y_i) is the position of the i-th cell, and w_j $(j = 1, 2)$ is the weight of each component of movement. The first term of the right-hand side represents Brownian motion where dw_x and dw_y are the increments obeying Gaussian distribution $N(0, dt)$, respectively. In the second term, U is a potential energy for generating the force of contact repulsion, and, in particular, we used the following quadratic function:

$$U(r_{i,j}) = \begin{cases} \left(\frac{r_{i,j}}{L} - 1\right)^2 & (0 < r_{i,j} \leq L) \\ 0 & (L < r_{i,j}) \end{cases},$$

where $r_{i,j}$ is the center-to-center distance between cell i and j. The contact repulsion between cells is assumed to occur when the intercellular distance is within L, and its effect is stronger when the distance is smaller, which was implemented not as an "all or none" response but as a response showing an inverse linear relationship with intercellular distance. The value of L was determined by the sum of mean sizes of cell body and filopodia (specifically, we used L = 55 (μm) in the simulations) (see also the Supplemental Experimental Procedures).

For experimental procedures on tissue preparation, in situ hybridization, immunohistochemistry, anterograde labeling, and quantifications, see the Supplemental Experimental Procedures.

SUPPLEMENTAL INFORMATION

Supplemental Information includes Supplemental Experimental Procedures, six figures, and five movies and can be found with this article online at http://dx.doi.org/10.1016/j.cub.2015.08.028.

AUTHOR CONTRIBUTIONS

Y.A. and Y.M. contributed equally to this work. M.B. and A.P. conceived the study. M.B. carried out most of the experiments. Y.A. and Y.M. designed and performed the mathematical simulations, L.V. the arealization analysis, F.C. early regionalization analysis and VAMP2 immunostaining, U.B. microarrays and MATLAB analysis, E.C. and F.L. analysis of late CR distribution, S.G. and D.J. anterograde labeling and vGlut2 staining and analysis, and V.C. participated in the analysis with the Imaris software. V.P.-G. and T.G. provided expertise on VAMPs and membrane trafficking, *Vamp3* mutant mice and helped designing the experiments. F.W.P. provided the B6;FVB-Tg(CAGboNT/B,EGFP and F.T. the *DeltaNp73* mouse lines. M.B., Y.M., Y.A., V.P.-G., T.G., D.J., and A.P. wrote the manuscript. A.P. supervised the project. All authors discussed and edited the manuscript.

ACKNOWLEDGMENTS

We acknowledge the ImagoSeine facility, member of the France BioImaging infrastructure supported by the Agence Nationale de la Recherche (ANR) (ANR-10-INSB-04, "Investmentsfit the future") for help with confocal and time-lapse microscopy, and N. Boggetto for FACS sorting. We thank A. Dutriaux and Animalliance for technical assistance and animal care and S. Garel and C. Desplan for critical reading of the manuscript. M.B. was the recipient of a fellowship from *NeRF* (Neuropôle de recherche francilien), Y.A. from ARC (Association pour la Recherche sur le Cancer) and FRM (Fondation pour la Recherche Médicale), U.B. from *NeRF* and FRM, F.L. from Ile de France region DIM Cerveau et Pensée. A.P. is a CNRS (Centre National de la Recherche Scientifique) Investigator and member Team of the École des Neurosciences de Paris Ile-de-France (ENP). This work was supported by grants from the ANR (ANR-2011-BSV4-023-01), FRM («Equipe FRM DEQ20130326521»), Ville de Paris (2006 ASES 102), ARC (Project ARC no. SFI20111203674) and Fédération pour la Recherche sur le Cerveau (FRC) to A.P.; from Fondation Médicale Reine Elisabeth (FMRE) and Fondation JED Belgique to F.T.; and from INSERM, Association Française contre les Myopathies (AFM), ARC, Mairie de Paris Medical Research and Health Program, FRM and ENP to T.G.

Received: March 26, 2015
Revised: July 1, 2015
Accepted: August 13, 2015
Published: September 17, 2015

REFERENCES

1. Buckner, R.L., and Krienen, F.M. (2013). The evolution of distributed association networks in the human brain. Trends Cogn. Sci. *17*, 648–665.
2. Borello, U., and Pierani, A. (2010). Patterning the cerebral cortex: traveling with morphogens. Curr. Opin. Genet. Dev. *20*, 408–415.
3. O'Leary, D.D., Chou, S.J., and Sahara, S. (2007). Area patterning of the mammalian cortex. Neuron *56*, 252–269.
4. Chou, S.J., Babot, Z., Leingärtner, A., Studer, M., Nakagawa, Y., and O'Leary, D.D. (2013). Geniculocortical input drives genetic distinctions between primary and higher-order visual areas. Science *340*, 1239–1242.
5. Pouchelon, G., Gambino, F., Bellone, C., Telley, L., Vitali, I., Lüscher, C., Holtmaat, A., and Jabaudon, D. (2014). Modality-specific thalamocortical inputs instruct the identity of postsynaptic L4 neurons. Nature *511*, 471–474.
6. del Río, J.A., Martínez, A., Fonseca, M., Auladell, C., and Soriano, E. (1995). Glutamate-like immunoreactivity and fate of Cajal-Retzius cells in the murine cortex as identified with calretinin antibody. Cereb. Cortex *5*, 13–21.
7. Hevner, R.F., Neogi, T., Englund, C., Daza, R.A., and Fink, A. (2003). Cajal-Retzius cells in the mouse: transcription factors, neurotransmitters, and birthdays suggest a pallial origin. Brain Res. Dev. Brain Res. *141*, 39–53.
8. Ina, A., Sugiyama, M., Konno, J., Yoshida, S., Ohmomo, H., Nogami, H., Shutoh, F., and Hisano, S. (2007). Cajal-Retzius cells and subplate neurons differentially express vesicular glutamate transporters 1 and 2 during development of mouse cortex. Eur. J. Neurosci. *26*, 615–623.

9. D'Arcangelo, G., Miao, G.G., Chen, S.C., Soares, H.D., Morgan, J.I., and Curran, T. (1995). A protein related to extracellular matrix proteins deleted in the mouse mutant reeler. Nature *374*, 719–723.
10. Ogawa, M., Miyata, T., Nakajima, K., Yagyu, K., Seike, M., Ikenaka, K., Yamamoto, H., and Mikoshiba, K. (1995). The reeler gene-associated antigen on Cajal-Retzius neurons is a crucial molecule for laminar organization of cortical neurons. Neuron *14*, 899–912.
11. D'Arcangelo, G. (2005). The reeler mouse: anatomy of a mutant. Int. Rev. Neurobiol. *71*, 383–417.
12. Supèr, H., Del Río, J.A., Martínez, A., Pérez-Sust, P., and Soriano, E. (2000). Disruption of neuronal migration and radial glia in the developing cerebral cortex following ablation of Cajal-Retzius cells. Cereb. Cortex *10*, 602–613.
13. Soriano, E., Alvarado-Mallart, R.M., Dumesnil, N., Del Río, J.A., and Sotelo, C. (1997). Cajal-Retzius cells regulate the radial glia phenotype in the adult and developing cerebellum and alter granule cell migration. Neuron *18*, 563–577.
14. Kupferman, J.V., Basu, J., Russo, M.J., Guevarra, J., Cheung, S.K., and Siegelbaum, S.A. (2014). Reelin signaling specifies the molecular identity of the pyramidal neuron distal dendritic compartment. Cell *158*, 1335–1347.
15. Del Río, J.A., Heimrich, B., Borrell, V., Förster, E., Drakew, A., Alcántara, S., Nakajima, K., Miyata, T., Ogawa, M., Mikoshiba, K., et al. (1997). A role for Cajal-Retzius cells and reelin in the development of hippocampal connections. Nature *385*, 70–74.
16. Caronia-Brown, G., and Grove, E.A. (2011). Timing of cortical interneuron migration is influenced by the cortical hem. Cereb. Cortex *21*, 748–755.
17. Anstötz, M., Cosgrove, K.E., Hack, I., Mugnaini, E., Maccaferri, G., and Lübke, J.H. (2014). Morphology, input-output relations and synaptic connectivity of Cajal-Retzius cells in layer 1 of the developing neocortex of CXCR4-EGFP mice. Brain Struct. Funct. *219*, 2119–2139.
18. Kilb, W., and Luhmann, H.J. (2001). Spontaneous GABAergic postsynaptic currents in Cajal-Retzius cells in neonatal rat cerebral cortex. Eur. J. Neurosci. *13*, 1387–1390.
19. Sava, B.A., Dávid, C.S., Teissier, A., Pierani, A., Staiger, J.F., Luhmann, H.J., and Kilb, W. (2010). Electrophysiological and morphological properties of Cajal-Retzius cells with different ontogenetic origins. Neuroscience *167*, 724–734.
20. Soda, T., Nakashima, R., Watanabe, D., Nakajima, K., Pastan, I., and Nakanishi, S. (2003). Segregation and coactivation of developing neocortical layer 1 neurons. J. Neurosci. *23*, 6272–6279.
21. Meyer, G., Goffinet, A.M., and Fairén, A. (1999). What is a Cajal-Retzius cell? A reassessment of a classical cell type based on recent observations in the developing neocortex. Cereb. Cortex *9*, 765–775.
22. Takiguchi-Hayashi, K., Sekiguchi, M., Ashigaki, S., Takamatsu, M., Hasegawa, H., Suzuki-Migishima, R., Yokoyama, M., Nakanishi, S., and Tanabe, Y. (2004). Generation of reelin-positive marginal zone cells from the caudomedial wall of telencephalic vesicles. J. Neurosci. *24*, 2286–2295.
23. Bielle, F., Griveau, A., Narboux-Nême, N., Vigneau, S., Sigrist, M., Arber, S., Wassef, M., and Pierani, A. (2005). Multiple origins of Cajal-Retzius cells at the borders of the developing pallium. Nat. Neurosci. *8*, 1002–1012.
24. Yoshida, M., Assimacopoulos, S., Jones, K.R., and Grove, E.A. (2006). Massive loss of Cajal-Retzius cells does not disrupt neocortical layer order. Development *133*, 537–545.
25. Griveau, A., Borello, U., Causeret, F., Tissir, F., Boggetto, N., Karaz, S., and Pierani, A. (2010). A novel role for Dbx1-derived Cajal-Retzius cells in early regionalization of the cerebral cortical neuroepithelium. PLoS Biol. *8*, e1000440.
26. Tissir, F., Ravni, A., Achouri, Y., Riethmacher, D., Meyer, G., and Goffinet, A.M. (2009). DeltaNp73 regulates neuronal survival in vivo. Proc. Natl. Acad. Sci. USA *106*, 16871–16876.
27. Villar-Cerviño, V., Molano-Mazón, M., Catchpole, T., Valdeolmillos, M., Henkemeyer, M., Martínez, L.M., Borrell, V., and Marín, O. (2013). Contact repulsion controls the dispersion and final distribution of Cajal-Retzius cells. Neuron *77*, 457–471.
28. Proux-Gillardeaux, V., Rudge, R., and Galli, T. (2005). The tetanus neurotoxin-sensitive and insensitive routes to and from the plasma membrane: fast and slow pathways? Traffic *6*, 366–373.
29. Chilcote, T.J., Galli, T., Mundigl, O., Edelmann, L., McPherson, P.S., Takei, K., and De Camilli, P. (1995). Cellubrevin and synaptobrevins: similar subcellular localization and biochemical properties in PC12 cells. J. Cell Biol. *129*, 219–231.
30. Galli, T., Chilcote, T., Mundigl, O., Binz, T., Niemann, H., and De Camilli, P. (1994). Tetanus toxin-mediated cleavage of cellubrevin impairs exocytosis of transferrin receptor-containing vesicles in CHO cells. J. Cell Biol. *125*, 1015–1024.
31. Proux-Gillardeaux, V., Gavard, J., Irinopoulou, T., Mège, R.M., and Galli, T. (2005). Tetanus neurotoxin-mediated cleavage of cellubrevin impairs epithelial cell migration and integrin-dependent cell adhesion. Proc. Natl. Acad. Sci. USA *102*, 6362–6367.
32. Skalski, M., Yi, Q., Kean, M.J., Myers, D.W., Williams, K.C., Burtnik, A., and Coppolino, M.G. (2010). Lamellipodium extension and membrane ruffling require different SNARE-mediated trafficking pathways. BMC Cell Biol. *11*, 62.
33. Veale, K.J., Offenhäuser, C., Whittaker, S.P., Estrella, R.P., and Murray, R.Z. (2010). Recycling endosome membrane incorporation into the leading edge regulates lamellipodia formation and macrophage migration. Traffic *11*, 1370–1379.
34. Riggs, K.A., Hasan, N., Humphrey, D., Raleigh, C., Nevitt, C., Corbin, D., and Hu, C. (2012). Regulation of integrin endocytic recycling and chemotactic cell migration by syntaxin 6 and VAMP3 interaction. J. Cell Sci. *125*, 3827–3839.
35. Veale, K.J., Offenhäuser, C., Lei, N., Stanley, A.C., Stow, J.L., and Murray, R.Z. (2011). VAMP3 regulates podosome organisation in macrophages and together with Stx4/SNAP23 mediates adhesion, cell spreading and persistent migration. Exp. Cell Res. *317*, 1817–1829.
36. Bacci, A., Coco, S., Pravettoni, E., Schenk, U., Armano, S., Frassoni, C., Verderio, C., De Camilli, P., and Matteoli, M. (2001). Chronic blockade of glutamate receptors enhances presynaptic release and downregulates the interaction between synaptophysin-synaptobrevin-vesicle-associated membrane protein 2. J. Neurosci. *21*, 6588–6596.
37. Zylbersztejn, K., Petkovic, M., Burgo, A., Deck, M., Garel, S., Marcos, S., Bloch-Gallego, E., Nothias, F., Serini, G., Bagnard, D., et al. (2012). The vesicular SNARE Synaptobrevin is required for Semaphorin 3A axonal repulsion. J. Cell Biol. *196*, 37–46.
38. Tojima, T., Akiyama, H., Itofusa, R., Li, Y., Katayama, H., Miyawaki, A., and Kamiguchi, H. (2007). Attractive axon guidance involves asymmetric membrane transport and exocytosis in the growth cone. Nat. Neurosci. *10*, 58–66.
39. Slezak, M., Grosche, A., Niemiec, A., Tanimoto, N., Pannicke, T., Münch, T.A., Crocker, B., Isope, P., Härtig, W., Beck, S.C., et al. (2012). Relevance of exocytotic glutamate release from retinal glia. Neuron *74*, 504–516.
40. Cholfin, J.A., and Rubenstein, J.L. (2007). Patterning of frontal cortex subdivisions by Fgf17. Proc. Natl. Acad. Sci. USA *104*, 7652–7657.
41. Lee, S.M., Tole, S., Grove, E., and McMahon, A.P. (2000). A local Wnt-3a signal is required for development of the mammalian hippocampus. Development *127*, 457–467.
42. Yang, C., Mora, S., Ryder, J.W., Coker, K.J., Hansen, P., Allen, L.A., and Pessin, J.E. (2001). VAMP3 null mice display normal constitutive, insulin- and exercise-regulated vesicle trafficking. Mol. Cell. Biol. *21*, 1573–1580.
43. Chiara, F., Badaloni, A., Croci, L., Yeh, M.L., Cariboni, A., Hoerder-Suabedissen, A., Consalez, G.G., Eickholt, B., Shimogori, T., Parnavelas, J.G., and Rakić, S. (2012). Early B-cell factors 2 and 3 (EBF2/3) regulate early migration of Cajal-Retzius cells from the cortical hem. Dev. Biol. *365*, 277–289.
44. Borrell, V., and Marín, O. (2006). Meninges control tangential migration of hem-derived Cajal-Retzius cells via CXCL12/CXCR4 signaling. Nat. Neurosci. *9*, 1284–1293.

45. Bribián, A., Nocentini, S., Llorens, F., Gil, V., Mire, E., Reginensi, D., Yoshida, Y., Mann, F., and del Río, J.A. (2014). Sema3E/PlexinD1 regulates the migration of hem-derived Cajal-Retzius cells in developing cerebral cortex. Nat. Commun. *5*, 4265.

46. Tojima, T., Itofusa, R., and Kamiguchi, H. (2014). Steering neuronal growth cones by shifting the imbalance between exocytosis and endocytosis. J. Neurosci. *34*, 7165–7178.

47. Zhou, P., Porcionatto, M., Pilapil, M., Chen, Y., Choi, Y., Tolias, K.F., Bikoff, J.B., Hong, E.J., Greenberg, M.E., and Segal, R.A. (2007). Polarized signaling endosomes coordinate BDNF-induced chemotaxis of cerebellar precursors. Neuron *55*, 53–68.

48. Liu, Y.J., Le Berre, M., Lautenschlaeger, F., Maiuri, P., Callan-Jones, A., Heuzé, M., Takaki, T., Voituriez, R., and Piel, M. (2015). Confinement and low adhesion induce fast amoeboid migration of slow mesenchymal cells. Cell *160*, 659–672.

49. Joslin, E.J., Opresko, L.K., Wells, A., Wiley, H.S., and Lauffenburger, D.A. (2007). EGF-receptor-mediated mammary epithelial cell migration is driven by sustained ERK signaling from autocrine stimulation. J. Cell Sci. *120*, 3688–3699.

50. Sekine, K., Kubo, K., and Nakajima, K. (2014). How does Reelin control neuronal migration and layer formation in the developing mammalian neocortex? Neurosci. Res. *86*, 50–58.

51. Courtès, S., Vernerey, J., Pujadas, L., Magalon, K., Cremer, H., Soriano, E., Durbec, P., and Cayre, M. (2011). Reelin controls progenitor cell migration in the healthy and pathological adult mouse brain. PLoS ONE *6*, e20430.

52. Vázquez-Carretero, M.D., García-Miranda, P., Calonge, M.L., Peral, M.J., and Ilundain, A.A. (2014). Dab1 and reelin participate in a common signal pathway that controls intestinal crypt/villus unit dynamics. Biol. Cell *106*, 83–96.

53. Gross, J.C., Chaudhary, V., Bartscherer, K., and Boutros, M. (2012). Active Wnt proteins are secreted on exosomes. Nat. Cell Biol. *14*, 1036–1045.

54. Caronia-Brown, G., Yoshida, M., Gulden, F., Assimacopoulos, S., and Grove, E.A. (2014). The cortical hem regulates the size and patterning of neocortex. Development *141*, 2855–2865.

55. Kwon, H.J., Ma, S., and Huang, Z. (2011). Radial glia regulate Cajal-Retzius cell positioning in the early embryonic cerebral cortex. Dev. Biol. *351*, 25–34.

56. Wallace, M.T., Ramachandran, R., and Stein, B.E. (2004). A revised view of sensory cortical parcellation. Proc. Natl. Acad. Sci. USA *101*, 2167–2172.

57. Donoghue, J.P., Kerman, K.L., and Ebner, F.F. (1979). Evidence for two organizational plans within the somatic sensory-motor cortex of the rat. J. Comp. Neurol. *183*, 647–663.

Current Biology

Supplemental Information

Migration Speed of Cajal-Retzius Cells Modulated by Vesicular Trafficking Controls the Size of Higher-Order Cortical Areas

Melissa Barber, Yoko Arai, Yoshihiro Morishita, Lisa Vigier, Frédéric Causeret, Ugo Borello, Fanny Ledonne, Eva Coppola, Vincent Contremoulins, Frank W. Pfrieger, Fadel Tissir, Subashika Govindan, Denis Jabaudon, Véronique Proux-Gillardeaux, Thierry Galli, and Alessandra Pierani

Supplemental Figures and Legends

Figure S1.

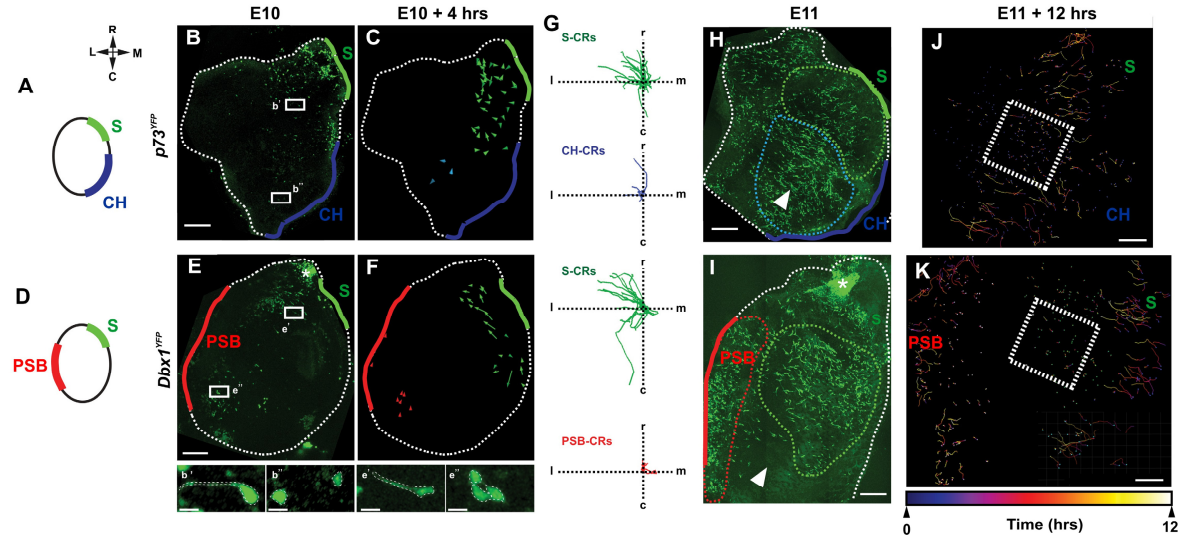

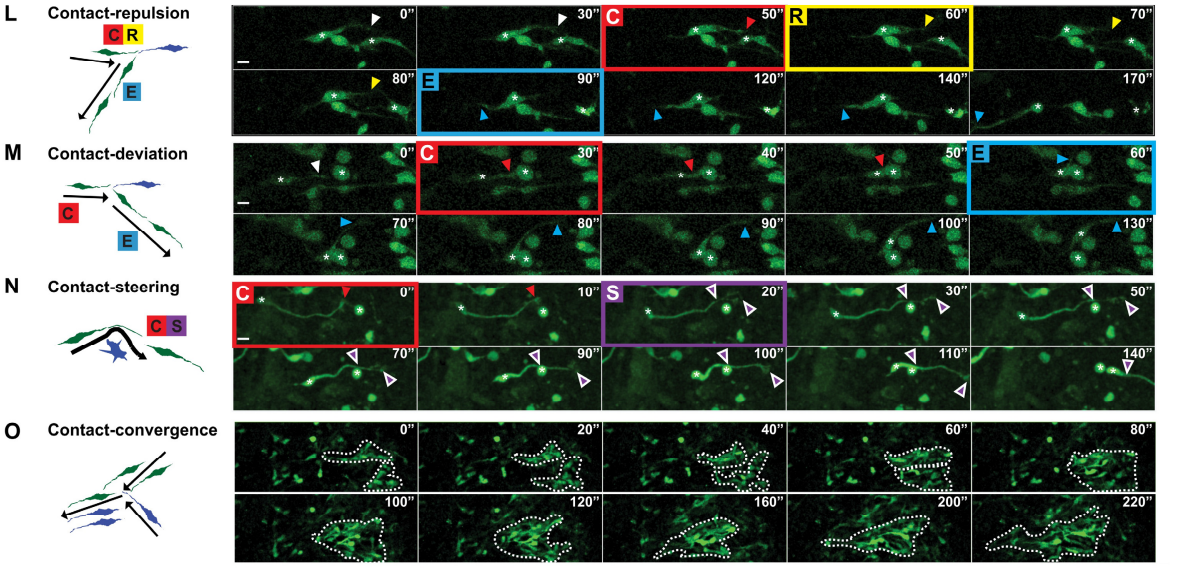

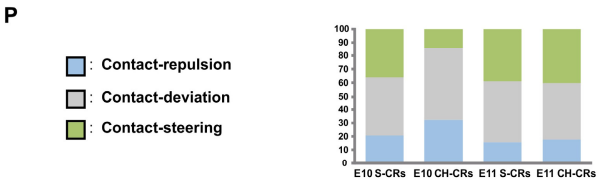

Figure S2.

A

Probe ID	Gene	Signal DM	Signal DL	Ratio DM/DL
1421863_at	**Vamp1**	78,45	64,66	1,20±0,11
1420834_at	**Vamp2**	327,77	620,78	0,53±0,10
1433916_at	**Vamp3**	511,28	308,23	1,69±0,23
1456245_x_at	**Vamp3**	2376,30	1544,23	1,59 ±0,25
1437708_x_at	**Vamp3**	3550,69	2568,70	1,40±0,15
1422895_at	**Vamp4**	960,54	745,11	1,30±0,10
1422896_at	**Vamp4**	42,15	35,20	1,21±0,12
1434796_at	**Vamp4**	322,99	379,77	0,85±0,08
1430522_a_at	**Vamp5**	35,33	41,33	0,87±0,11
1426269_at	**Vamp7**	425,76	506,15	0,87±0,22
1452007_at	**Vamp7**	201,71	254,31	0,79±0,07
1420624_a_at	**Vamp8**	80,78	42,17	2,11±0,74
1420897_at	**Snap23**	128,81	72,06	1,80±0,20
1420898_at	**Snap23**	37,71	33,91	1,15±0,20
1416828_at	**Snap25**	211,06	528,22	0,40±0,04
1438176_x_at	**Snap47**	3420,77	5794,01	0,59±0,11
1423745_at	**Snap47**	545,52	1121,67	0,51±0,14
1437817_at	**Snap91**	26,42	38,00	0,75±0,22
1416688_at	**Snap91**	633,46	1058,16	0,62±0,12
1437390_x_at	**Stx1a**	897,02	1469,71	0,61±0,17
1448366_at	**Stx1a**	67,88	86,92	0,88±0,28
1438780_at	**Stx1b**	129,34	185,98	0,74±0,18
1418164_at	**Stx2**	294,24	250,92	1,19±0,10
1425536_at	**Stx3**	1100,04	458,56	2,97±1,19
1434559_at	**Stx3**	91,84	33,10	2,82±1,13
1425530_a_at	**Stx3**	103,07	45,17	2,33±0,73
1451573_a_at	**Stx4a**	166,80	103,42	1,63±0,19

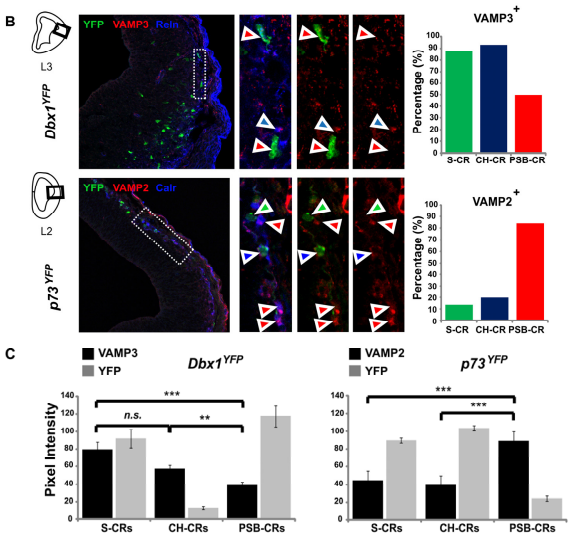

Figure S3.

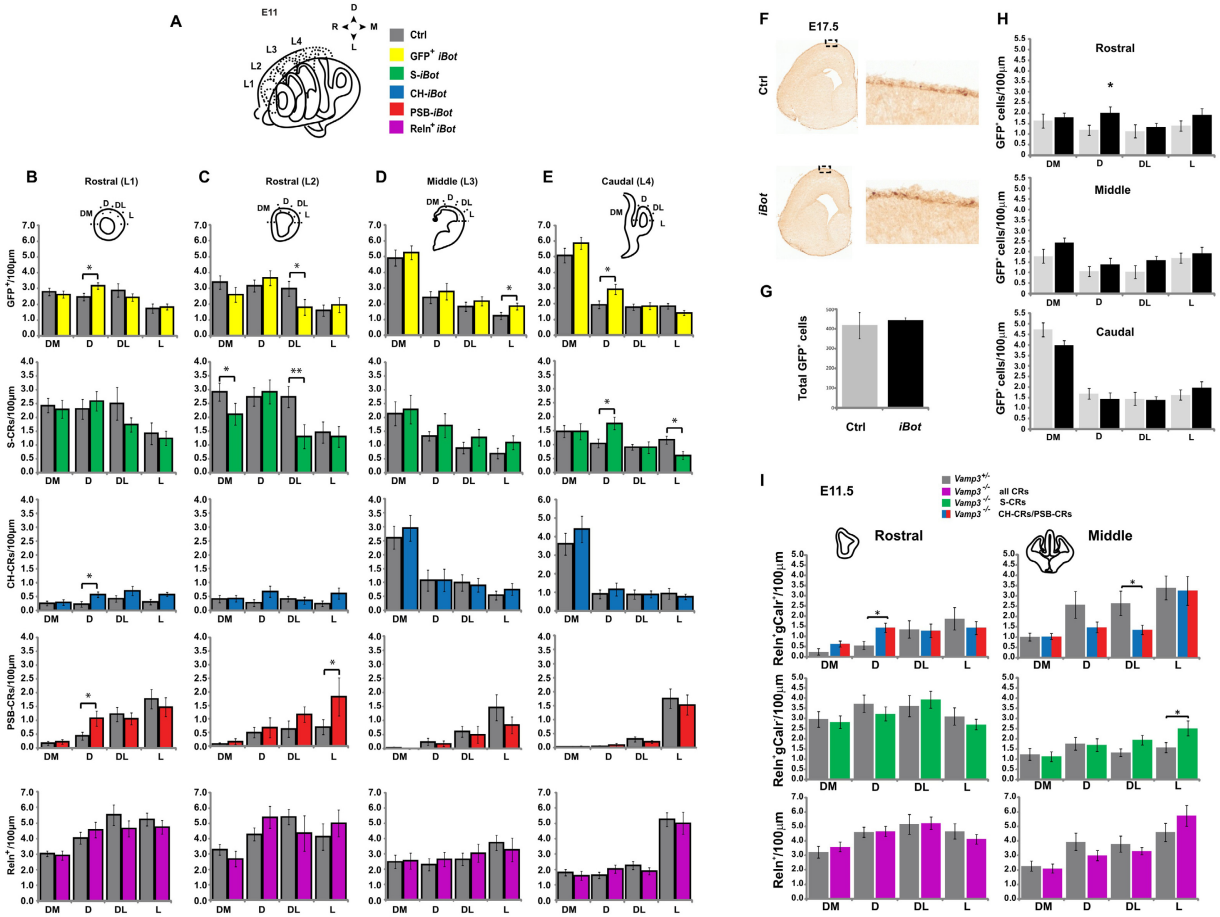

Figure S4.

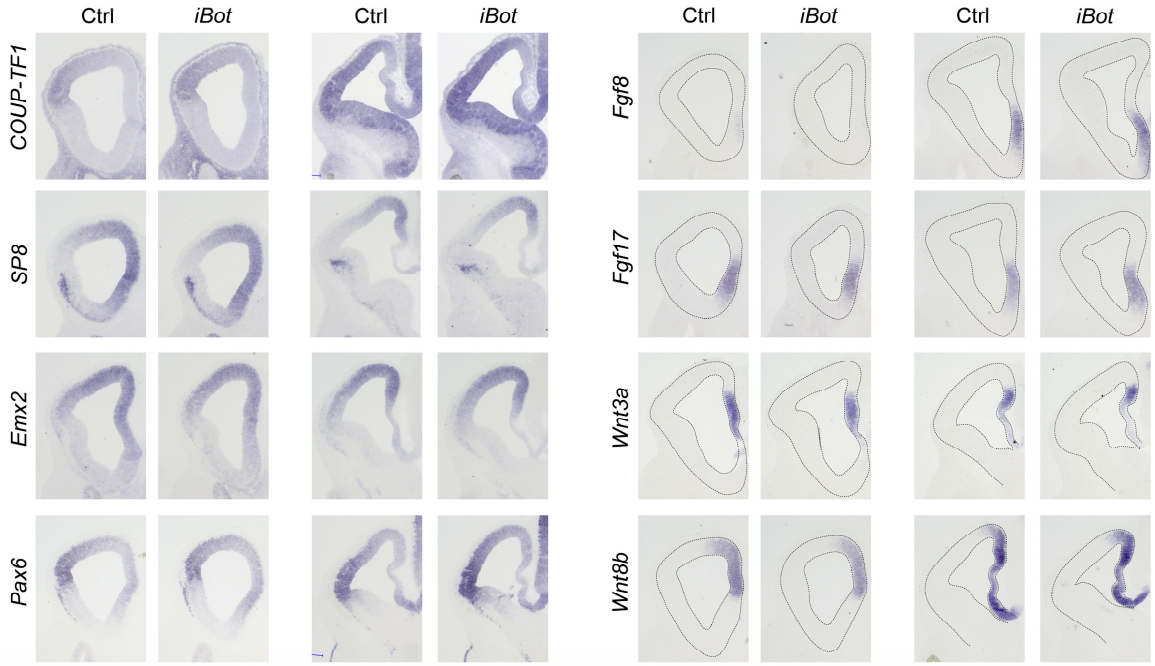

Figure S5.

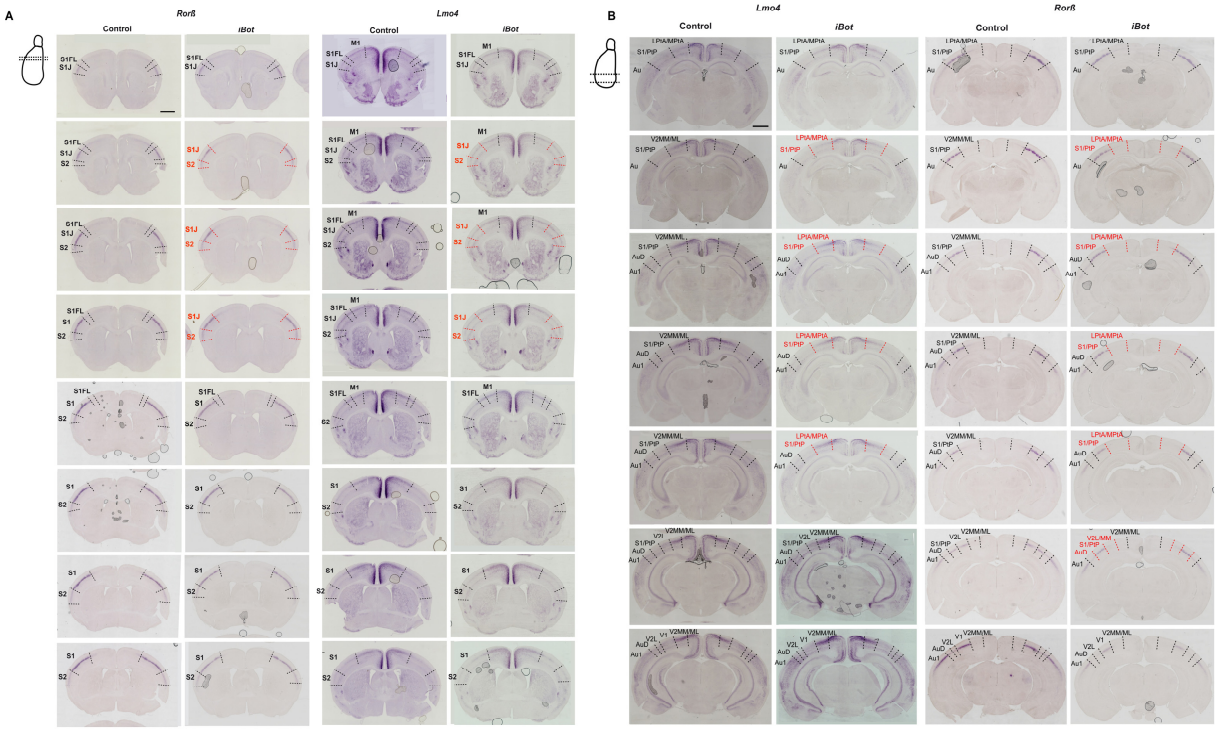

Figure S6.

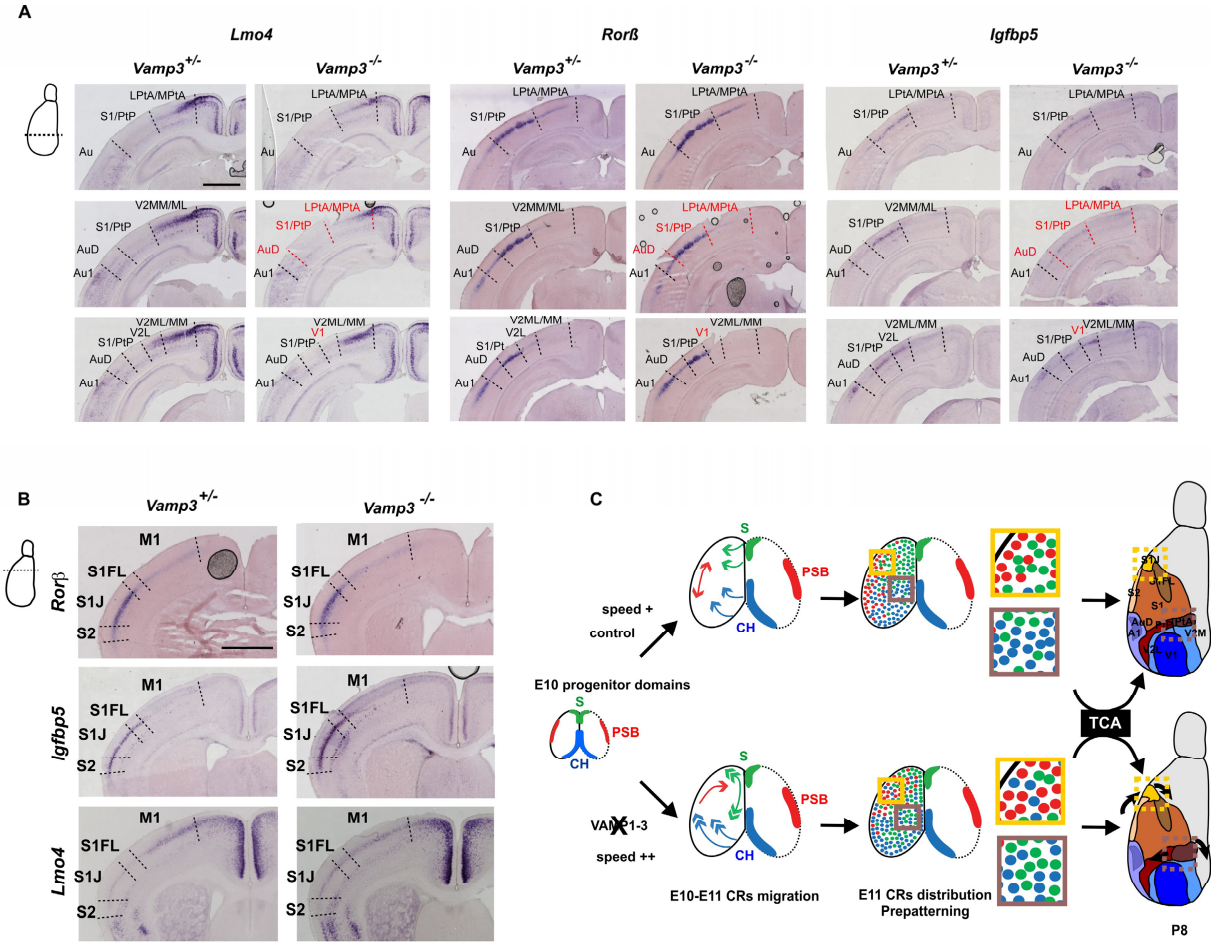
A
Lmo4
Rorß
Igfbp5
Vamp3+/-
Vamp3-/-
LPtA/MPtA
S1/PtP
Au
V2MM/ML
AuD
Au1
V2ML/MM
V2L
V1
B
Vamp3+/-
Vamp3 -/-
Rorβ
Igfbp5
Lmo4
M1
S1FL
S1J
S2
C
speed +
control
E10 progenitor domains
S
PSB
CH
VAMP1-3
speed ++
E10-E11 CRs migration
E11 CRs distribution
Prepatterning
TCA
P8

Figure S1. Related to Figure 1. (A-K) Whole-flattened cortical preparations at E10-E11 and live imaging. (A, D) Progenitor domains in flattened cortices from the $p73^{YFP}$ (A) and the $Dbx1^{YFP}$ (D) mouse lines. Rostral is up and medial is right. (**B, E, H, I**) Confocal z-stack projections of E10 (B, E) and E11 (H, I) cortical preparations after 4 hrs in culture showing the first frame of time-lapse acquisition (T=0) from $p73^{YFP}$ (B, H) and $Dbx1^{YFP}$ (E, I) embryos. Magnification of boxed regions in B, E show migrating S-CRs with polarized morphologies in the rostral cortex (B', E') and not migrating rounded CH-CRs (B") and PSB-CRs (E") in the caudal and lateral cortex. **(C, F)** Displacement vectors showing minimum distance between start and end position of CRs tracked for 4 hrs in $p73^{YFP}$ (C) and $Dbx1^{YFP}$ (F) explants at E10. S-CRs: green arrows in C (n=40) and F (n=37), CH-CRs: blue arrows (n=8) and PSB-CRs: red arrows (n=11). **(G)** Representative trajectories of CRs at E10 clustered at a common starting point and plotted for their displacement along the rostral(r)-caudal(c) and medial(m)-lateral(l) axes to display their directionality. S-CRs: green tracks in $p73^{YFP}$ (n=17) and $Dbx1^{YFP}$ (n=12); CH-CRs: blue tracks (n=8); PSB-CRs red tracks (n=11). S-CRs from $p73^{YFP}$ and $Dbx1^{YFP}$ mouse lines display similar migration kinetics. (**H, I**) Confocal z-stack projections of E11 at T=0 showing regional distribution of CR subtypes: S-CRs (green dashed outlines in H, I), CH-CRs (blue dashed outlines in H and arrowheads in H, I) and PSB-CRs (red dashed outline in I). Asterisks indicate extrapallial territories. **(J, K)** Total trajectories of YFP^+ cells imaged over 12hrs from E11 $p73^{YFP}$ and $Dbx1^{YFP}$ flattened cortices colour coded for time (blue is timeframe 0 and white is end of the time-lapse). Scale bars: 200µm (B, E, J), 10µm (B', B", E', E"), 300µm (H, I). **(L-P) Contact-redistribution of CR subtypes comprises heterogeneous behaviors. (L-O)** High resolution time-lapse sequence of migrating CRs in flattened whole-mount preparations of E11.5 cortices from $p73^{YFP}$ mice, showing distinct behaviors of CRs following cell-contact with other YFP^+ CRs. Scored behaviors were: **(L)** contact-repulsion when contact with another CR cell resulted in the full retraction of their leading process and re-extension of a new leading process from a distinct position within the cell to deviate by >90° from their original path; **(M)** contact-deviation when contact resulted in partial retraction and branching of the leading process to deviate by <90° from the original trajectory; **(N)** contact-steering when contact resulted in steering of their leading process without retraction to deviate around adjacent cells. C in red box: contact; E in blue box: extension; R in yellow box: retraction; S in purple box: steering. Contacting cells are labeled with an asterisk. Arrowheads show point of contact. (**O**) Convergence of directional migratory streams was specifically observed in the rostro-medial cortex (contact-convergence). **(P)** Quantification of observed behaviors for S-CRs and CH-CRs following cell-contact expressed as a percentage of total cell contacts at E10 and at E11. E10 S-CRs n=39, CH-CRs n=28; E11 S-CRs n=77; CH-CRs: n=50. No significant differences in distribution of behaviors were found between subtypes and stages using the χ^2 test.

Figure S2. Related to Figure 3. VAMP3 and VAMP2 are differentially expressed in S-CRs and PSB-CRs. (A) Expression profiles for genes of the exocytotic machinery in FACS-sorted *Dbx1*-derived S-CRs (DM) and PSB-CRs (DL). Values shown correspond to the mean normalized signal obtained from three separate microarray experiments. Genes were considered to be enriched in S-CRs when the mean-fold change was ≥1.4 relative to PSB-CRs (Ratio DM/DL). *Vamp3*, together with its t-SNARE partners involved in apical exocytosis in epithelial cells, *Syntaxin3* and *Snap23*, are specifically enriched in S-CRs compared to PSB-CRs. In contrast, *Vamp2*, together with its t-SNARE partners *Snap25*, and *Syntaxins1a/1b* are more highly expressed in PSB-CRs relative to S-CRs. Affymetrix probeset ID, gene name, signal value in DM and DL, ratios DM/DL. **(B)** Immunohistochemical analysis and quantifications of CR subtypes expressing VAMP3 and VAMP2 proteins in E11 $Dbx1^{YFP}$ and $p73^{YFP}$ developing rostro-lateral cortices, respectively. Schemas show coronal sections taken from rostral level 3 (top) and level 2 (bottom) along the anterior-posterior axis, respectively. Boxed regions are shown at high magnification in panels on the right. Top panels: immunostaining for VAMP3 (red), GFP (green) and Reln (blue) proteins, showing the colocalization of VAMP3 in GFP^-Reln^+ CH-CRs (blue arrowheads) and its low expression or absence in GFP^+Reln^+ PSB-CRs (red arrowheads). Bottom panels: immunostaining for VAMP2 (red), GFP (green) and Calr (blue) proteins, showing robust colocalisation of VAMP2 in GFP^-Calr^+ PSB-CRs (red arrowheads) and its low or absent expression in GFP^+Calr^- S-CRs and GFP^+Calr^+ CH-CRs (green and blue arrowheads). Graphs show quantifications of the percentage of CR subtypes expressing VAMP3 (top) (S-CRs: n=20/25, PSB-CRs: n=15/30, CH-CRs: n=38/40); or VAMP2 (bottom) (S-CRs: n=24/186, PSB-CRs: n=251/302, CH-CRs: n=65/339). **(C)** Graphical

representation of mean gray pixel values ± SEM for VAMP3 (black bars left panel), VAMP2 (black bars right panel) and GFP (grey bars) immunofluorescence intensity in CR subtypes. Quantifications for VAMP3 were made from S-CRs (n=25), PSB-CRs (n=30) and CH-CRs (n=11) and for VAMP2 from S-CRs (n=26), PSB-CRs (n=29) and CH-CRs (n=39). Student's t-Test; ** $p \leq 0.01$, *** $p \leq 0.001$, n.s.: not significant.

Figure S3. Related to Figure 4. (A-E) Redistribution of CR subtypes in the developing cerebral cortex of *iBot* mutants at E11. (A) Schemas of coronal sections quantified at rostral levels (L1 **(B)** and L2 **(C)**) and mid-caudal levels (L3 **(D)** and L4 **(E)**) along the rostral-caudal axis of the telencephalon. Quantifications of CR subtypes were performed from confocal images of E11 *p73^{Cre};iBot* (*p73;iBot*) and control (*p73^{YFP}*)embryos after immunohistochemical staining for GFP (green), Reln (red) and Calret (blue) (Figure 4). Grey and colored columns show counts in control (Ctrl) and *p73;iBot* mutants, respectively: GFP$^+$ (comprising both S-CRs and CH-CRs, yellow), S-CRs (GFP$^+$Reln$^+$, green), CH-CRs (GFP$^+$Reln$^+$gCalr$^+$ and single GFP$^+$ (corresponding to later born CH-CRs which show delayed expression of Reln$^+$gCalr$^+$, blue)), PSB-CRs (GFP$^-$Reln$^+$gCalr$^+$, red) and all CRs (Reln$^+$, purple). Schemas in B-E indicate subdivisions along the medial-lateral axis for each section quantified at L1-L4 levels. DM: dorsal-medial, D: dorsal, DL: dorsal-lateral, L: lateral. Graphical representation of normalized cell counts (cells/100µm ± SEM) (n=3 brains for each genotype). Student's t-Test; * $p \leq 0.05$, ** $p \leq 0.01$. **(F-H) Altered distribution of CR subtypes in *iBot* at E17.5.** (**F**) Coronal sections taken at rostral level 1 of an E17.5 control *p73^{Cre}* (top) and *p73^{Cre};iBot* mutant (bottom) forebrain showing the immunolocalization of GFP$^+$ *p73*-derived CRs (S-CRs and CH-CRs). Boxed regions, corresponding to the marginal zone of the dorsal cortex, are shown at high magnification in panels on the right. **(G)** Total numbers of GFP$^+$ (cells ± SEM) in E17.5 control (n=3) (grey bars) and *p73^{Cre};iBot* mutant (n=3) (black bars) forebrains, quantified from rostral, middle and caudal sections of the telencephalon. **(H)** Quantifications of *p73*-derived CR subtypes (GFP$^+$ cells/100µm ± SEM) at rostral, middle and caudal levels of E17.5 control (n=3 brains) (grey bars) and *p73;iBot* mutant (n=3 brains) (black bars). The cortex was divided along the medial-lateral axis into four regions at each levels and show a redistribution of S-CRs and CH-CRs in the rostral dorsal cortex. Student's T-test * $p<0.05$. **(I) Altered distribution of CR subtypes in *Vamp3* null mutants.** Quantification of CR subtypes at rostral and mid-caudal levels (cells/100µm ± SEM) in E11 *Vamp3* mutants (-/-) compared to controls (+/-, grey): Reln$^+$gCalr$^+$ (CH-CRs and PSB-CRs: blue/red), Reln$^+$gCalr$^-$ (S-CRs: green) and Reln$^+$ (all CRs: purple) (n=3 brains for each genotype). At rostral levels the number of Reln$^+$gCalr$^+$ cells was increased in the dorsal cortex of *Vamp3* mutants whereas it was decreased in the dorso-lateral cortex at mid-caudal levels. At this level Reln$^+$gCalr$^-$ were found in higher number in the lateral mutant cortex. No changes were observed in total Reln$^+$ cells in mutant sections relative to controls showing a redistribution of CR subtypes. Student's t-Test; * $p \leq 0.05$. DM: dorsal-medial; D: dorsal; DL: dorsal-lateral; L: lateral regions.

Figure S4. Related to Figure 5. Absence of changes in gene expression of early regionalization gradients and at signaling centers. *In situ* hybridization for *CoupTF1*, *Sp8*, *Emx2, Pax6*, *Fgf8*, *Fgf17*, *Wnt3a* and *Wnt8b* on E11.5 coronal sections of the telencephalon from *p73;iBot* mutants compared with control (Ctrl) littermates showing no detectable differences. Scale bar: 200 µm.

Figure S5. Related to Figure 5. (A) Changes in the size of the somatosensory secondary cortex along the rostral cortex in *iBot* mutants. *In situ* hybridization on coronal sections of P8 control and *iBot* mutants using *Rorβ* and *Lmo4* mRNA probes at rostral levels along the rostro-caudal axis, with corresponding levels shown in schematic on the top left. Black dashed lines indicate areal borders and red dashed lines show dorsal displacement of S1J and enlargement of S2 in mutants relative to controls. Defects are observed from level 2 to 4 corresponding to an extent of 300 µm. At level 5 S1FL is present in mutants as in controls. S1J: primary somatosensory cortex jaw region; S1FL: primary somatosensory cortex forelimb region; S2: secondary somatosensory cortex; M1: primary motor cortex. **(B) Changes in the size of the parietal association and visual secondary cortex along the rostro-caudal axis in *iBot* mutants.** *In situ* hybridization on coronal sections of P8 control and *iBot* mutants using *Lmo4* and *Rorβ* mRNA probes at mid-caudal levels along the rostro-caudal axis, with corresponding levels shown in schematic on the top left. Black dashed lines indicate areal borders and red dashed lines the changes in mutants. Enlargement of

parietal association cortex and reduction of visual and auditory secondary cortex are observed from level 2 to 6, corresponding to an extent of 500 μm. V2ML/MM: secondary visual cortex mediolateral/mediomedial; LPtA/MPtA: lateral parietal association/medial parietal association cortex; S1/PtP: primary somatosensory/parietal association cortex posterior rostral and dorsal; AuD: auditory secondary cortex dorsal (AuD), Au1: primary auditory cortex; V2L: secondary visual cortex lateral; V1: primary visual cortex. Scale bar: 1 mm and applies to all panels.

Figure S6. Related to Figure 6. Expansion of the parietal association cortex and primary somatosensory/posterior parietal association cortical areas at the expense of the secondary visual and auditory cortex in *Vamp3* null mutants. (A, B) *In situ* hybridization on coronal sections of P8 *Vamp3*$^{+/-}$ (control) and *Vamp3*$^{-/-}$ mutant brains using *Lmo4*, *Rorβ* and *Igfbp5* mRNA probes at mid-caudal (A) and rostral (B) levels. A replacement of V2ML/MM (characterized by *Lmo4*^{high} layer 3,5a/*Lmo4*^{low} layer 4,6 with no *Igfbp5* and *Rorβ*) by LPtA/MPtA (expressing *Lmo4* layer 4^{low},6/*Rorβ*^{low} layer 4) and an enlargement of S1/PtP (*Lmo4* layer 6/*Rorβ*^{high} layer 4/*Igfbp5* layer 3,5) at the expenses of AuD (*Lmo4* layer 4^{low},6/*Rorβ*^{low} layer 4/*Igfbp5*^{low} layer 3) are observed. A rostral extension of V1 (*Lmo4*^{low} layer 3,5a,6/*Rorβ*^{low} layer 4/*Igfbp5* layer 3) replacing V2L (*Lmo4*^{high} layer 3,5a,6/*Rorβ*^{low} layer 4/*Igfbp5* layer 3) is also detected. No differences in the position and size of M1, S1FL, S1J and S2 were observed (B). Black dashed lines indicate areal borders and red dashed lines the changes in mutants. S1/PtP: primary somatosensory/parietal association cortex posterior rostral and dorsal (PtPR/PtPD); LPtA/MPtA: lateral parietal association/medial parietal association cortex; V2ML/MM: secondary visual cortex mediolateral/mediomedial; V1: visual primary cortex; V2L: visual secondary lateral cortex; AuD: auditory secondary cortex dorsal; M1: primary motor cortex, S1FL: primary somatosensory cortex forelimb region, SIJ: primary somatosensory cortex jaw region, S2: secondary somatosensory cortex. Scale bar: 1 mm and applies to all panels. **(C)** Summary model: CRs migration speed regulates subtypes signaling activity in cortical territories to prepattern higher-order cortical areas. CR subtypes migrate from signaling centers at the borders of the developing cerebral cortex to cover complementary territories (S-CRs (green), CH-CRs (blue) and PSB-CRs (red)) and signal to progenitors to control their mode of division (Griveau et al., 2010). Genetically increasing S-CRs and CH-CRs migration speeds (++) through VAMP3 inactivation results in their invasion of more distant cortical territories (double green and blue arrowheads). This changes the composition and signaling activity of CRs in rostro-lateral and caudo-medial territories at E11 and, in turns, alters the size of higher-order cortical areas located in the rostro-lateral and caudo-medial cortex at P8. CR distribution would serve to prepattern cortical territories and guide afferents from the thalamus (TCA: Thalamo-cortical axons) which will later mediate refinement of patterning by sensory inputs.

Supplemental Experimental Procedures

Animals

DeltaNp73$^{CreiresEGFP/+}$ and *DeltaNp73*$^{CreiresEGFP/+}$;*ROSA26*$^{loxP\text{-}STOP\text{-}loxP\text{-}YFP}$ embryos did not show significant differences when immunostained with anti-GFP antibodies (recognizing both GFP and YFP) at E10-E12 indicating that the EGFP in the *DeltaNp73* locus allows to account for all CRs of the DeltaNp73 lineage at these stages. Explants obtained by crossing *Dbx1*$^{iresCre/+}$ mice with the *iBot* line could not be imaged due to low GFP and decreased viability of the explants. Embryos and postnatal animals were genotyped by PCR using primers specific for the different alleles as previously described [S1, S2].

Tissue Preparation, In Situ Hybridization and Immunohistochemistry

For staging of embryos, midday of the vaginal plug was considered as embryonic day 0.5 (E0.5). Embryos for immunohistochemistry were fixed by immersion in 4% paraformaldehyde (PFA), 0.1 M phosphate buffer (PB) pH 7.2 for 2 hrs at 4°C and rinsed in PBS for 4 hrs at 4°C. Postnatal animals were anesthetized with 40-70 mg/kg of pentobarbital sodique (Ceva Santé Animale) and perfused with 20 ml of 4% PFA for 5 min. Postnatal brains for *in situ* hybridisation were further post-fixed in 4% PFA, 0.1M phosphate buffer overnight at 4°C. Embryonic and postnatal brains were cryoprotected for 24 and 48 hrs, respectively, in 30% sucrose, 0.1 M PB and embedded in O.C.T. compound (Tissue Tek). Embedded tissues were sectioned on a cryostat with a 14 µm step for embryonic stages and 50 µm for postnatal brains. *In situ* hybridization was performed as previously described [S3]. RNA probes for *in situ* hybridization used in this study were mouse *CoupTF1*, *Sp8*, *Emx2, Pax6*, *Fgf8*, *Fgf17*, *Wnt3a*, *Wnt8b, Igfbp5, Lmo4* and *Rorβ.* Serial sections from each P8 brain were processed with 2 or 3 mRNA probes. Immunohistochemistry on sections was performed as previously described [S4]. Primary antibodies used were mouse G10 anti-Reln (Calbiochem; 1:1000), rabbit anti-GFP (Molecular Probes; 1:1000), goat anti-Calr (SWANT 1:250), rabbit anti-Calr (SWANT 1:1000; for Figure S2B and C), rabbit anti-human TG1 VAMP3 (1:200), mouse anti-VAMP2 (mAb Cl69.1, Synaptic Systems, 1:100) and guinea-pig anti-VGLUT2 (1:2000, Millipore, AB2251). Fluorescent secondary antibodies used were Cy3 donkey anti-mouse (Jackson; 1:700), Cy5 donkey anti-goat (Jackson; 1:500), Alexa 488 donkey anti-chick (Jackson; 1:1000). Nuclei were counterstained with 4′,6-diamidino-2-phenylindole (DAPI) (Sigma, 2.5 µg/ml).

Anterograde labeling

Anterograde labeling from the VPM thalamic nucleus was performed on P8 brains as previously described [S5]. Briefly, the caudal part of fixed P8 brains was cut to reveal the caudal thalamus. Trypan blue staining was applied to allow distinction between thalamic nuclei and anterograde labeling was initiated by insertion of small NeuroVue Dye-coated Filter Red (MTTI, FS-1002) (50 3 50 mm2) in the VB nucleus. Brains were incubated at 37^{o}C in 0.4% PFA for 8 weeks and cut into 100-mm sections on a vibratome before immediate imaging.

Counts and intensity quantifications of VAMP proteins

VAMP2- and VAMP3-expressing CR subtypes were characterized using immunohistochemistry on coronal sections taken from E11.5 *DeltaNp73*$^{CreiresEGFP/+;}$*ROSA26*$^{loxP\text{-}STOP\text{-}loxP\text{-}YFP}$ and *Dbx1*$^{iresCre/+;}$*ROSA26*$^{loxP\text{-}STOP\text{-}loxP\text{-}YFP}$ embryonic mouse forebrains. *Dbx1*^{YFP} sections were immunostained for YFP, Reln and VAMP3 and cell counts were obtained for Dbx1^{YFP+}Reln^{+} S-CRs in the dorsal-medial and dorsal cortex at rostral levels 1 and 2 (L1-L2) (n=25 cells), Dbx1^{YFP+}Reln^{+} PSB-CRs counted in the dorsal-lateral cortex in rostral sections at L2 to L3 (n= 30) and Dbx1^{YFP-}Reln^{+} CH-CRs counted in the dorsal-medial and dorsal cortex at caudal levels (n=40). *P73*^{YFP} sections were immunostained for YFP, Calr and VAMP2 and cell counts were obtained for p73^{YFP+} S-CRs in the dorsal-medial cortex at rostral L1 (n=186 cells), p73^{YFP-}Calr^{+} PSB-CRs in the dorsal-lateral cortex at rostral L2 (n= 302) and p73^{YFP+}Calr^{+} CH-CRs in the dorsal-medial cortex at caudal level (n=339). Mean grey pixel values corresponding to measurements of intensity of VAMP2, VAMP3 and YFP staining were obtained from raw confocal 1 μm single-z images acquired with the 40x oil objective and with identical laser settings for each. VAMP2, VAMP3 and YFP proteins were detected with an Alexa568-conjugated and Alexa488-conjugated secondary antibody, respectively, and excited at 488nm and 568nm wavelengths, with mean gray pixel values calculated from single channel images as a measure of VAMP staining intensity. As VAMP3 staining was particulate in nature, the multi-pointer selection tool in Image J software was used to select 3 regions of interest for each cell where possible, and mean gray values obtained using the Image J analyze module. Measurements for VAMP2 and YFP were obtained using the same method. VAMP3 and YFP mean pixel intensity measurements were averaged from n=25 S-CRs, n=30 PSB-CRs and n=11 CH-CRs and VAMP2 and YFP pixel intensity measurements were taken from n=26 S-CRs, n=29 PSB-CRs and n=39 CH-CRs in the same cortical regions as described for cell counts.

Quantifications of CR subtypes in *Vamp3* null and *p73;iBot* mutants

CR subtypes were quantified at embryonic stages (E11.5) from confocal acquired images of rostral, middle and caudal coronal sections with 3 brains analysed for each genotype. Analysis of GFP^{+} CRs traced in *p73*^{Cre}*;Ibot* and *p73*^{Cre} control brains at E17.5 were quantified from brightfield images acquired from coronal sections at rostral, middle and caudal levels of the forebrain. For all, the cortex was subdivided into four regions along its dorsal-medial and lateral axis and counts scored using the cell-counter tool with Image J software.

Whole flattened cerebral cortical preparations

The telencephalic vesicles were separated at the midline and the diencephalic tissue removed medially. Two incisions were made medially to detach the pallial septum and the cortical hem from the ventral territories and open the vesicle cup. At E10, as the ganglionic eminences (GE) were not morphologically discernible, the ventral telencephalon was not excised to ensure that the laterally positioned PSB was present in these preparations. There was little risk of contamination from subpallial sources of Dbx1-derived cortical interneurons at this stage as these initiate their migration from E11 [S6]. Incisions were made at mid-points on the rostro-caudal axis medially and laterally to flatten the explants. At E11, ventral subpallial tissue was removed by making incisions mid-way along

the lateral GE to preserve the PSB progenitor domain. Incisions were further made 1) mid-way along the medial axis between the S and CH and 2) mid-way along the lateral axis to flatten the explants. Flattened whole cortices were cultured with the ventricular surface of the explants adjacent to the membrane. Immediately before imaging, the flattened cortical explants were transferred with the underlying Millicell membranes and inverted onto a bespoke glass-bottom microscope imaging chamber with the pial surface directly adjacent to the glass-bottom, and secured by adding 100 µl of purified bovine collagen (Advanced Biomatrix) which was polymerized at 37°C and 5% CO_2. This provides a system which preserves the meninges and a 3-D migratory environment required for maintaining CRs in the marginal zone *in vivo* [S7]. Each preparation allows for simultaneous analysis of CRs migrating from two spatially distinct progenitor domains located at the edges of the explants towards the dorsal pallium. Data from *Dbx1*^{YFP} embryos was used to represent S-CRs in Figure 1C, D and F to exclude possible overlap with CH-CRs migrating along the medial axis.

Live imaging confocal microscopy and image acquisition

Inverted confocal microscopy (Leica 710 and Leica 780) was used for live-image acquisition over 4-14 hrs of cortical explants maintained at 37°C and 5% CO_2 in a regulated chamber. YFP and GFP proteins were excited at 514nm and at 488nm wavelengths, respectively. Composite tile scan images ranged from 2x2 to 5x3 to enable imaging of the entire pallium of different staged embryos at a frame rate of 1/10 min on a total z-depth range of 30-70 µm from the pial surface using a 25x or a 40x oil objective. While acquisitions along the z-axis varied between explants due to differences in flattening of the curved telencephalic vesicles, the YFP and GFP signal was consistently confined within a maximum depth of 30 µm i.e. ~3 cell diameters and therefore considered comparable across time-lapse sequences. Brightfield images of brain sections were acquired using a colour camera (Zeiss Axiocam HRc) coupled to a Zeiss Axiovert 200 microscope. Composites of brightfield images were acquired using the AxioVision 4.6 software with Mosaix and Tiling options, which automatically acquires multiple images of the same specimen and reconstructs the final image. Position of cortical areas was determined using the Atlas of the Developing Mouse Brain (P6) (Paxinos, Halliday, Watson, Koutcherov and Wang, Academic Press) and The Mouse Brain (adult) (Franklin and Paxinos, Academic Press).

Data collection and statistical analysis of time-lapse images

For all experiments, cell tracks have been obtained from at least three whole flattened brains imaged 4-14 hours at each stage (E10-E10.5, E11-11.5) and for each genotype, except for PSB-CRs at E10 as only two brains contained active migration from the PSB at this stage. All tracking analysis was carried out on z-projections. The trajectories of migrating CR subtypes, which were ≥50 µm from the edge of the explant were selected to eliminate edge artifacts due to flattening of the explant during the imaging period. Cells were considered to be actively migrating if their displacement track length was ≥35 µm. YFP$^+$ (and GFP$^+$ for *iBot*) CRs were automatically tracked using the spot module on the Imaris Bitplane software (*Version 6.1)*. Erroneous tracks were manually corrected to quantify the speed and persistence in directionality of migrating CRs and to obtain positional information of their displacement along the x and y co-ordinates. CRs were tracked for variable durations due to loss of cells from the z-plane of focus

during the imaging period. However, the tracking duration of cells ranged between 4-12 hrs. Tracing CRs with the *Dbx1*^{YFP} mouse line enabled pure populations for S- and PSB-CR subtypes to be selected for based on spatial exclusion of the progenitor domains which were located at the medial and lateral edges, respectively, of the explant. When tracking cells in *p73*^{YFP} cortical explants we selected CRs migrating from the caudal medial edge of the explant corresponding to CH-CRs, and excluded CRs migrating from the rostral and middle levels of the explant to reduce contamination from S-CRs. The mean speed, directionality index (DI), and displacement vectors were automatically calculated for each cell during the time series, using the Imaris software spot module function. Mean speed was determined by measuring the total length of a cell's trajectory (μm) and dividing this by duration of the trajectory (secs) throughout the time series; displacement vectors represent the shortest distance between the start and end position of a cell's trajectory (μm); DI is the ratio between displacement vectors and the total path length (μm). The overall directionality in migration was determined by automatic clustering of tracks to a common origin using the Imaris transpose tracks function. Clustered tracks were plotted along the x and y axis using the Imaris Vantage module to generate 2-d vectorial displacement of tracks with cells clustered at a common origin. For all quantifications, mean values ± SEM are shown and statistical analysis was performed using a Student's unpaired two-tailed T-test since all sets of data followed a Gaussian distribution. For quantifications in Figure S1 contacts between two cells were scored if occurring within a single optical slice from *Dbx1*^{YFP} (for S-CRs) and *p73*^{YFP} (for CH-CRs) explants in the rostral and caudal cortex, respectively, (n=2 brains for each genotype at both E10 and E11, except for *Dbx1*^{YFP} at E10 n=3 brains). The angle of deviation was calculated using the Image J software and the Imaris cell-tracking spot module. Statistical analysis of the scored contact-redistribution behaviors was carried out using a Pearson's chi-squared test.

Mathematical simulations of the dynamics of CR cell distribution

1-1. Calculation of tissue shape and each progenitor domain

To model the tissue shape accurately, an average ellipsoid shape (1,100 μm in length and 800 μm in width) from four different samples of flattened preparations at E10 was used to represent the surface area of the cerebral cortex. Each CR progenitor domain was demarcated based on both results of *in situ* hybridization and immunostaining for *p73* and *Dbx1* expression to estimate the percentage occupancy of each progenitor domain on the averaged ellipsoid shape of the cortical explant. In the case of E11+24 hrs simulation (*Ibot* control and mutant) in models 7 and 8 (see Summary of mathematical models below and Figure 3I), we used the same average ellipsoid shape obtained from E10. The growth of tissue and surface area of cortical explants over the imaging period were measured by manually delineating the contours of whole explants at the beginning and end of the time-lapse using the Fiji software. Superimposition of the contours showed minimal growth of explants in culture over the imaging period (1.18% Surface Area increase, n=13 explants from E10 and E11) (data not shown) considered to be negligible for the mathematical simulation. Potential artefacts caused by tissue drift, which creates false movements of cells, were corrected by manually tracking displacement of edges and debris in tissue using the spot module of Imaris software (Carl Zeiss) in the brightfield and eliminated from the analyses.

1-2. Supply of cells from each progenitor domain

Cells of each CR subtype were supplied from their sources (i.e. Septum, Cortical hem or PSB) into the dorsal pallium every 2 minutes. Total cells supplied: 2160 cells (720 S-CRs, 720 PSB-CRs and 720 CH-CRs each) in 24 hrs (model 1 in Summary below and Figure 2A), 1800 cells (720 S-CRs, 540 PSB-CRs and 540 CH-CRs each) in 24 hrs (models 4 in Summary below and Figure 2B, 3I), 2160 cells (720 S-CRs, 720 PSB-CRs and 720 CH-CRs each) in 30 hrs (Figure 2D), 1800 cells (720 S-CRs, 540 PSB-CRs and 540 CH-CRs each) in 24 hrs (Figure 2E), 2160 cells (720 S-CRs, 720 PSB-CRs and 720 CH-CRs each) in 24 hrs (model 2, 3 in Summary below and Figure 2F, G and H), 2160 cells (720 S-CRs, 720 PSB-CRs and 720 CH-CRs each) in 30 hrs (Figure 2I) and 1800 cells (720 S-CRs, 540 PSB-CRs and 540 CH-CRs each) in 24 hrs (model 5, 6 in Summary below and Figure 2J and K) from the beginning of the mathematical simulation (see Summary of Mathematical Models below and Figure 2). This was based on the counting of the total number of CRs (1883±80 cells, mean total number from two explants) using $p73^{YFP}$ and $Dbx1^{YFP}$ explants at E10.5 processed for Reln, Calretinin and YFP immunohistochemistry after a 12 hr imaging period, considered to be equivalent to E11, and $p73^{YFP}$ and $Dbx1^{YFP}$ explants prepared at E11 corresponding to time zero prior to imaging.

1-3. Mathematical simulation using different kinetics

Using the above basic information, we performed different mathematical simulations including the experimentally obtained parameters: (i) onset of migration, (ii) mean speed of each CR subtype, and (iii) persistence in directionality (Directionality index; DI) (see below for summary). First, onset of migration was determined by the degree of the appearance of YFP^+ CRs from their progenitor domains using $p73^{YFP}$ and $Dbx1^{YFP}$ explants obtained from E10, E10.25, E10.5 and E10.75 and according to their size of the telencephalon. Second, the cell migration was modeled by the weighted sum of two components: (i) random motion (walking) and (ii) contact repulsion between cells. Parameters for equivalent kinetics models were determined from the mean speed and DI values taken across all three subtypes. Parameters of migration kinetics for S-CRs and PSB-CRs were determined from experimental time-lapse data from E10 $Dbx1^{YFP}$ cortical explants and for CH-CRs from $p73^{YFP}$ explants (n=3).

Two weighting coefficients for random walking (W_1) and for contact repulsion (W_2) were determined so as to reproduce the experimentally obtained mean speed of migration and persistence in directionality for all models. The value of W_2 for each subtype was used to calculate the effect of contact repulsion among the same subtypes (homotypic weighing coefficients) (see Summary of mathematical models below), however, once different subtypes contacted each other on the way of migration, we chosen the following W_2 values as a heterotypic weighting coefficient so that different CR subtypes are moderately mixed as observed *in vivo*: (i) Figure 2B (model 4 Summary of mathematical models below), H and I, S-CH: 0.2 x (W_2 of S) + 0.8 x (W_2 of CH) = 11.4, S-PSB: 0.1 x (W_2 of S) + 0.9 x (W_2 of PSB) = 3.62, PSB-CH: 0.5 x (W_2 of PSB) + 0.5 x (W_2 of CH) = 3.9, (ii) Figure 2J (model 5 Summary of mathematical models below), S-CH: 0.2 x (W_2 of S) + 0.8 x (W_2 of CH) = 0.74, S-PSB: 0.1 x (W_2 of S) + 0.9 x (W_2 of PSB) = 0.53, PSB-CH: 0.5 x (W_2 of PSB) + 0.5 x (W_2 of CH) = 0.53, (iii) Figure 2K (model 6 Summary of mathematical models below), S-CH: 0.2 x (W_2 of S) + 0.8 x (W_2 of CH) = 2.5, S-PSB: 0.1 x (W_2 of S) + 0.9 x (W_2 of PSB) = 0.8, PSB-CH: 0.5 x (W_2 of PSB) + 0.5 x (W_2 of CH) = 1.38, (iv) Figure 3I (model 7 Summary of mathematical models below), S-CH: 0.2 x (W_2 of S) + 0.8 x (W_2 of CH) = 6.0, S-PSB: 0.1 x (W_2 of S) + 0.9 x (W_2 of PSB) = 1.52, PSB-CH: 0.5 x (W_2 of PSB) + 0.5 x (W_2 of CH) = 3.15, (v) Figure 3I (model 8 Summary of mathematical models below), S-CH: 0.2 x (W_2 of S) + 0.8 x (W_2 of CH) = 11.4, S-PSB: 0.1 x (W_2 of S) + 0.9 x (W_2 of PSB) = 2.42, PSB-CH: 0.5 x (W_2 of PSB) + 0.5 x (W_2 of CH) = 5.4. In the case of equivalent kinetics simulations, the values of W_1 and W_2 are determined so as to reproduce the average of mean speeds and mean persistence in directionality from all three CR subtypes at E10 and W_2 heterotypic weighting coefficient values of each combination was 5 (model 1 Summary of mathematical models below and Figure 2A, D, E), 0.75 (model 2 Summary of mathematical models below and Figure 2F) and 1.5 (model 3 Summary of mathematical models below and Figure 2G) equivalent to the homotypic weighting coefficient.

Summary of mathematical models

		Onset	Mean speed (μm/h)	DI	Homotypic weighting coefficients	
					Random walking (w1)	Contact repulsion (w2)
Model 1	Equivalent kinetics Fig. 2A & Movie S3 (*left panel*)	=	20	0.51	0.85	5.0
Model 2	Equivalent kinetics Fig. 2F	=	20	0.255	0.9	0.75
Model 3	Equivalent kinetics Fig. 2G	=	10	0.51	0.4	1.5
Model 4	CR subtype kinetics + onset Fig. 2B & Movie S3 (*right panel*)	≠	S-CRs: 28.0 PSB-CRs: 13.5 CH-CRs: 18.7	0.67 0.31 0.54	0.9 0.6 0.7	29.0 0.8 7.0
Model 5	CR subtype kinetics + onset Fig. 2J	≠	S-CRs: 28.0 PSB-CRs: 13.5 CH-CRs: 18.7	0.255 0.255 0.255	1.22 0.6 0.81	1.26 0.45 0.61
Model 6	CR subtype kinetics + onset Fig. 2K	≠	S-CRs: 10 PSB-CRs: 10 CH-CRs: 10	0.67 0.31 0.54	0.3 0.45 0.375	3.5 0.5 2.25
Model 7	*iBot*-Control Fig. 3I & Movie S5 (*left panel*)	≠	S-CRs: 21.1 PSB-CRs: 13.5 CH-CRs: 17.2	0.55 0.31 0.57	0.8 0.6 0.7	8.0 0.8 5.5
Model 8	*iBot*-Mutant Fig. 3I & Movie S5 (*right panel*)	≠	S-CRs: 26.8 PSB-CRs: 13.5 CH-CRs: 22.8	0.59 0.31 0.58	1.0 0.6 0.9	17.0 0.8 10.0

Mathematical simulations. Summary of mathematical simulations based on kinetics' data obtained from live-imaging studies at E10 (models 1 and 6), and from time-lapse analysis of control and *iBot* mutant cortical flattened preparations at E11 (models 7 and 8). Onset of migration: (=) equal onset, (≠) S-CRs initiate migration 6 hrs prior to PSB-CRs and CH-CRs; DI: persistence in directionality. For each subtype, the cell migration was modeled by the weighted sum of two components: (i) random walking *(w1)* and (ii) contact repulsion *(w2)* between cells. When different subtype cells meet each other, we used heterotypic weighting coefficients (see Supplemental Experimental Procedures for details on the parameter settings). In model 1, CRs migrate at equivalent speeds (20μm/hr) and DI

(0.51) determined by averaging values from all three CR subtypes in E10 time-lapses (n=3 explants). In model 4, control values for S-CR and PSB-CR kinetics were obtained from *Dbx1*^{YFP} time-lapses, and control CH-CR from *p73*^{YFP} time-lapses at E10. Control PSB-CR values were obtained from *Dbx1*^{YFP} time-lapses in models 7, 8, with control S-CR and CH-CR from *p73*^{YFP} time-lapses in model 7 and S-*iBo*t and CH-*iBot* kinetics from *iBot* timelaspes in model 8 (n=3 explants). The individual parameters changed in models 2, 3, 5 and 6 are DI (models 2 and 5) and mean speed (models 3 and 6).

Supplemental References

S1. Bielle, F., Griveau, A., Narboux-Neme, N., Vigneau, S., Sigrist, M., Arber, S., Wassef, M., and Pierani, A. (2005). Multiple origins of Cajal-Retzius cells at the borders of the developing pallium. Nat Neurosci *8*, 1002-1012.

S2. Slezak, M., Grosche, A., Niemiec, A., Tanimoto, N., Pannicke, T., Munch, T.A., Crocker, B., Isope, P., Hartig, W., Beck, S.C., et al. (2012). Relevance of exocytotic glutamate release from retinal glia. Neuron *74*, 504-516.

S3. Griveau, A., Borello, U., Causeret, F., Tissir, F., Boggetto, N., Karaz, S., and Pierani, A. (2010). A novel role for Dbx1-derived Cajal-Retzius cells in early regionalization of the cerebral cortical neuroepithelium. PLoS Biol *8*, e1000440.

S4. Pierani, A., Moran-Rivard, L., Sunshine, M.J., Littman, D.R., Goulding, M., and Jessell, T.M. (2001). Control of interneuron fate in the developing spinal cord by the progenitor homeodomain protein Dbx1. Neuron *29*, 367-384.

S5. Pouchelon, G., Gambino, F., Bellone, C., Telley, L., Vitali, I., Luscher, C., Holtmaat, A., and Jabaudon, D. (2014). Modality-specific thalamocortical inputs instruct the identity of postsynaptic L4 neurons. Nature *511*, 471-474.

S6. Gelman, D., Griveau, A., Dehorter, N., Teissier, A., Varela, C., Pla, R., Pierani, A., and Marin, O. (2011). A wide diversity of cortical GABAergic interneurons derives from the embryonic preoptic area. J Neurosci *31*, 16570-16580.

S7. Borrell, V., and Marin, O. (2006). Meninges control tangential migration of hem-derived Cajal-Retzius cells via CXCL12/CXCR4 signaling. Nat Neurosci *9*, 1284-1293.